

Internal Hydraulic Transition and Turbulent Mixing Observed in the Kuroshio over the I-Lan Ridge off Northeastern Taiwan

MING-HUEI CHANG,^{a,b} YU-HSIN CHENG,^c YU-YU YEH,^a YIING JANG YANG,^{a,b} SEN JAN,^a CHIH-LUN LIU,^d TAKESHI MATSUNO,^e TAKAHIRO ENDOH,^e EISUKE TSUTSUMI,^f JIA-LIN CHEN,^g AND XINYU GUO^h

^a *Institute of Oceanography, National Taiwan University, Taipei, Taiwan*

^b *Ocean Center, National Taiwan University, Taipei, Taiwan*

^c *Department of Marine Environmental Informatics, National Taiwan Ocean University, Keelung, Taiwan*

^d *College of Earth, Ocean, and Atmospheric Sciences, Oregon State University, Corvallis, Oregon*

^e *Research Institute for Applied Mechanics, Kyushu University, Fukuoka, Japan*

^f *Atmosphere and Ocean Research Institute, University of Tokyo, Tokyo, Japan*

^g *Department of Hydraulic and Ocean Engineering, National Cheng Kung University, Tainan, Taiwan*

^h *Center for Marine Environmental Studies, Ehime University, Ehime, Japan*

(Manuscript received 28 October 2021, in final form 3 July 2022)

ABSTRACT: Complex small-scale processes and energetic turbulence are observed at a sill located on the I-Lan Ridge that spans across the strong Kuroshio off Taiwan. The current speed above the sill is strong (1.5 m s^{-1}) and unsteady ($\pm 0.5 \text{ m s}^{-1}$) due to the Kuroshio being modulated by the semidiurnal tide. Above the sill crest, isothermal domes, with vertical scales of ~ 20 and $\sim 50 \text{ m}$ during the low and high tides, respectively, are generated by turbulent mixing as a result of shear instability in the bottom boundary layer. Tidally modulated hydraulic character modifies the small-scale processes occurring on the leeward side of the sill. Criticality analysis, performed by solving the Taylor–Goldstein equation, suggests that the observed lee waves and intermediate layer sandwiched by two free shear layers are related to the mode-1 and mode-2 critical control between the sill crest and immediate lee, respectively. Around high tide, lee waves are advected further downstream, and only mode-1 critical control can occur, leading to a warm water depression. The shear instabilities ensuing from the hydraulic transition processes continuously mediate flow kinetic energy to turbulence such that the status of marginal instability where the Richardson number converges at approximately 0.25 is reached. The resultant eddy diffusivity K_p is concentrated from $O(10^{-4})$ to $O(10^{-3}) \text{ m}^2 \text{ s}^{-1}$ and has a maximum value of $10 \text{ m}^2 \text{ s}^{-1}$. The sill on the western flank of the Kuroshio is a hotspot for energetic mixing of Kuroshio waters and South China Sea waters.


KEYWORDS: Internal waves; Kelvin-Helmholtz instabilities; Small scale processes; Topographic effects; Turbulence

1. Introduction

The generation of turbulence by tidal and geostrophic flows over steep topography serves as a pathway for the energy cascade in the ocean where kinetic energy from winds and tides is transformed into microscale turbulent dissipation and mixing (Kunze et al. 2006; Nikurashin and Ferrari 2011). The transformation requires a downscale cascade from flow energy to microstructure turbulence ($< 1 \text{ m}$). The commonly seen small-scale processes that mediate the energy transformation include lee waves (Kunze and Lien 2019; Legg 2021) and hydraulic jumps (Farmer and Armi 1999; Wesson and Gregg 1994; Moum and Nash 2000; Nash and Moum 2001; Armi and Farmer 2002; Alford et al. 2013; Winters 2016) occurring in the immediate lee of the obstacle. These are too costly to be resolved in large-scale models. Therefore, parameterizing drag and turbulent mixing due to lee waves is required in oceanic and climate models (MacKinnon et al. 2017;

Kunze and Lien 2019; Moum 2021; Legg 2021). Fundamentally, a better understanding of these processes occurring at the subgrid scale is needed to improve physics-based parameterization schemes. As the small-scale processes generated by tidal flow over topography have been observed in greater detail than those driven by geostrophic flow (Legg 2021), in this paper, we examine the energetic small-scale processes that extract the geostrophic flow kinetic energy to near-field turbulence at a sill above the I-Lan Ridge in the strong Kuroshio northeast of Taiwan (Fig. 1a). As will be shown later, the Kuroshio flow speed is tidally modulated.

The Kuroshio is the western boundary current in the northern Pacific, which transports sizeable amounts of warm and salty water from the low-latitude to midlatitude ocean, modulates the global climate, and dominates regional ocean dynamics along its path. Its transport and maximum velocity axis are significantly modulated by mesoscale eddies (Lien et al. 2014; Jan et al. 2015; Cheng et al. 2017; Jan et al. 2017; Chang et al. 2018). Recent observations further revealed that flow interactions with abrupt topography along the Kuroshio main axis, e.g., headlands (Cheng et al. 2020), continental slopes (Endoh et al. 2016), seamounts (Chang et al. 2016), small reefs (Hasegawa et al. 2021), and islands (Chang et al. 2013; Hasegawa et al. 2004; Tsutsumi et al. 2017; Chang et al. 2019), are the primary sources of submesoscale vortical motions, which ultimately

 Denotes content that is immediately available upon publication as open access.

Corresponding author: Ming-Huei Chang, minghueichang@ntu.edu.tw

DOI: 10.1175/JPO-D-21-0245.1

© 2022 American Meteorological Society. For information regarding reuse of this content and general copyright information, consult the AMS Copyright Policy (www.ametsoc.org/PUBSReuseLicenses).

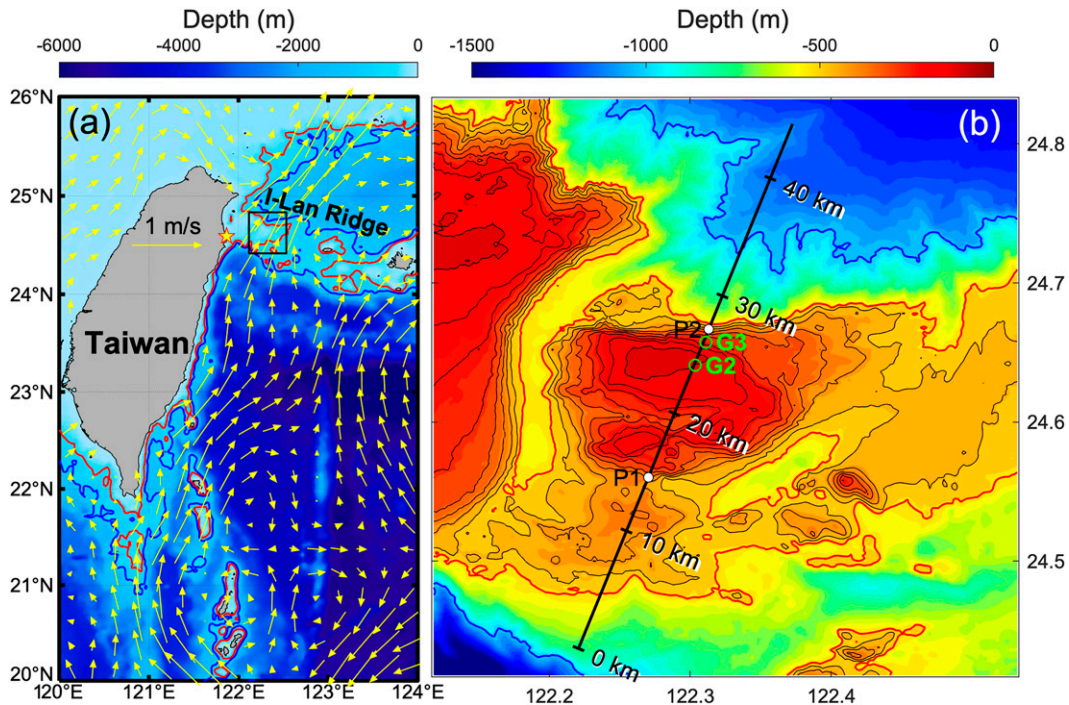


FIG. 1. (a) Bathymetry and surface current vectors around Taiwan derived from satellite absolute dynamic topography (ADT) on 11 May 2018. (b) Detailed bathymetry within the black box in (a), with the thick black line denoting the track of cross-sill (along-stream) surveys conducted during the 2021 cruise (Ex2). The red lines in (a) and (b) represent the 500-m isobath. The blue lines in (a) and (b) represent the 1000-m isobath. The thin black lines in (b) reflect isobaths from 50 to 500 m with an interval of 50 m. The Suao tidal station is denoted as a yellow star in (a). The locations of profiling station G2 and mooring G3 are denoted as the green circles in (b). The interval between P1 and P2 is the survey track in the 2018 cruise (Ex1).

lead to a downscale energy cascade and trigger turbulent mixing and dissipation. The near-inertial wave shear around topography also contributes to turbulence generation (Nagai et al. 2017). Enhanced turbulent mixing can extend ~ 100 km along the Kuroshio in the Tokara Strait (Nagai et al. 2021). In addition to its dynamical influences, the most striking biochemical effects of the resulting turbulence on the Kuroshio are 1) mixing could rapidly and significantly change the hydrographic properties of the Kuroshio, e.g., the modification of the subsurface salinity maximum (Tsutsumi et al. 2017), and 2) turbulent nitrate flux could promote production of phytoplankton (Kobari et al. 2020; Hasegawa et al. 2021; Acabado et al. 2021) in the oligotrophic Kuroshio.

The I-Lan Ridge spans the main path of the Kuroshio stream (Fig. 1b). The topographic passage on the I-Lan Ridge is known as the East Taiwan Channel (ETC), which is an entrance for the Kuroshio flowing into the East China Sea. The shallow shelves on the ridge characterized by the 500-m isobath (red curve in Fig. 1a) obstruct the Kuroshio and strongly affect the flow. Of particular interest are the small-scale processes on the shelf extending from Taiwan's coast (black box in Fig. 1a). Detailed bathymetry shows an isolated sill separated from the extended shelf by a narrow channel (Fig. 1b). The sill was selected as the targeting area in our experiments, where the Kuroshio flows at speeds varying between 1.5 and

2 m s^{-1} during our measuring period as a result of tidal modulation, presumably due to the generation of M_2 internal tides (Lien et al. 2013). The encounter of the strongly unsteady flow with the sill leads to the generation of a rich field of small-scale processes in the near field, fast evolution, and intense turbulent mixing that changes over time, which have rarely been observed before.

To gain an overall insight into the physical processes, we start by evaluating the nonlinearity of the stratified flow by estimating the lee wave Froude number (Aguilar and Sutherland 2006; Legg 2021)

$$\text{Fr}_L = Nh_0/U_0, \quad (1)$$

where N is the buoyancy frequency, h_0 is the vertical scale of the sill, and U_0 is the upstream flow speed. For $\text{Fr}_L < 1$, when the sill has a small height and/or stratification is weak, the lee waves are linear; therefore, the classic linear theory (Bell 1975) can be applied. In the regime of $\text{Fr}_L > 1$, the flow is characterized by partial blocking upstream and the generation of nonlinear lee waves, hydraulic control of the jet, and a stagnant wedge with well-mixed water downstream of the sill (Baines 1987; Winters 2016; Legg 2021). The flow kinetic energy is partly converted to a hydraulically controlled jet and dissipated in a hydraulic jump. According to our observations

upstream, Fr_L is 1.8–2.4, given $N \sim 0.012 \text{ s}^{-1}$, $h_0 \sim 300 \text{ m}$, and U_0 is $1.5\text{--}2 \text{ m s}^{-1}$, suggesting the likely presence of nonlinear lee waves, hydraulic jumps, and wedges of well-mixed layers. In this study, based on two field experiments, we analyze the flow criticality, detail the evolution of the hydraulic transition and lee wave, and quantify their resulting turbulent mixing underlying the strong and tidally modulated Kuroshio flow over a sill. The processes of lee wave breaking due to Kelvin–Helmholtz (KH) instability and flow advection above the sill crest are also presented. The significant modification of the hydrographic properties due to strong turbulent mixing are examined.

2. Experiments and data

Experiments were performed on two cruises conducted in May 2018 (Ex1) and May 2021 (Ex2) around the spring tide period. The first cruise (Ex1) was conducted on board R/V *Ocean Researcher 2 (OR2)*, and the second cruise (Ex2) was on board R/V *New Ocean Researcher 2 (NOR2)*. Overall, these measurements were focused on the 45-km cross-sill and along-stream transects (Fig. 1b). During Ex1, a subsurface mooring deployed at G3 in the immediate lee of the sill (Fig. 1b) was operational for 5 days (11–16 May). One upward-looking 600-kHz acoustic Doppler current profiler (ADCP) and one downward-looking 300-kHz ADCP were mounted on a main frame of the mooring at $\sim 80 \text{ m}$. The pair of ADCPs measured velocity profiles over 30–180 m with bin sizes of 2 and 4 m, respectively, every 30 s. Simultaneously, the mooring was equipped with 47 thermistors with a sampling interval of 10 s. Forty-three of the thermistors were attached to the mooring line distributed with a vertical resolution of 1–2 m spanning 85–165 m (red dots in Figs. 7a,d and 8a,d). Three of the four remaining thermistors were attached above 85 m and the remaining one was set below 165 m. A bottom-mounted mooring was simultaneously deployed at G2 but was not recovered due to unknown reasons. The hourly tidal sea levels recorded at a nearby tide gauge station Suao (indicated by a star sign in Fig. 1a), maintained by Taiwan's Central Weather Bureau, were used to indicate the tidal phase during our measuring period. Shipboard measurements of two transect surveys and station profiling were carried out in the period of moored measurements (as indicated by the horizontal lines in Fig. 4c). A 12.5-km transect from P1 to P2 (P1–P2 line) was chosen (Fig. 1b) for measurements, consisting of a shipboard ADCP (150-kHz TRDI ADCP) and echo sounder (120-kHz Simrad EK60) with sampling intervals of 1 min and 5 s, respectively. Shipboard time series stations were conducted at G2 (100 m) on the sill crest and G3 (220 m) in the immediate lee of the sill for $>24 \text{ h}$ using simultaneous shipboard measurements and turbulence profiles using a loosely tethered vertical microstructure profiler (VMP-500), manufactured by Rockland Scientific International, Inc. (RSI).

Three runs of shipboard surveys along the full 45-km transect (Fig. 1b) were performed in Ex2. Observations were taken using a combination of a shipboard 75-kHz ADCP and tow-yo turbulence profiler. The tow-yo turbulence profiler used was the vertical microstructure profiler-250 (VMP-250)

manufactured by RSI. The details for the operation can be found in Nagai et al. (2017) and Chang et al. (2021). In addition, temperature, conductivity, and fluorescence sensors were installed on the VMP-250, and the data were calibrated by a CTD cast that was profiled simultaneously. Microstructure profiles taken from VMP-500 (Ex1) and VMP-250 (Ex2) provided measurements of centimeter- to millimeter-scale shear so that the dissipation rate of turbulent kinetic energy (TKE) ϵ was estimated (see the appendix). The processing of the microstructure data and estimate of ϵ is based on the routines provided by RSI (ODAS; Douglas and Lueck 2015). In the following analysis, all measured currents are expressed as the cross-stream velocity u and along-stream velocity v obtained by rotating the coordinate system 22° (mean upstream current direction) clockwise.

3. Internal hydraulic control, shear instability, and turbulence

a. Hydrography and turbulence

Three repeated cross-sill surveys along the 45-km transect (Ex2; Fig. 1b) reveal remarkable discrepancies in temperature, salinity, and ϵ from the upstream to the downstream flow (Fig. 2). The temperature transects (Figs. 2a,d,g) show isothermal doming mostly above the crest of sill, followed by an isothermal depression. In the first and second surveys, there is a well-mixed layer below the depression. The salinity transect in the third survey (Fig. 2h) clearly demonstrates that the upstream flow could climb on the sill crest because the salinity maximum at $\sim 100\text{--}200 \text{ m}$ near the southern end of the transect (3 km) rises to 50–100 m above the sill crest. The salinity maximum (34.8–35 psu) at 100–200 m, a typical feature of West Philippines Sea Tropical Water (WPSTW) (Chen 2005; Mensah et al. 2014; Jan et al. 2015), disappears after the immediate lee of the sill. A similar spatial change in salinity distribution occurs in the second (Fig. 2e) and first (Fig. 2b) runs, but the breakpoint is shifted ahead of the sill.

The salinity within the isothermal dome is 34.5–34.6 psu, which is between 34.8 and 35 psu in the upstream layer of the salinity maximum and 34.3–34.4 in the upper layer above the sill (0–40 m). This suggests dramatic mixing processes occurred above the two sills. Indeed, a strong TKE dissipation rate ϵ ranging from $O(10^{-7})$ to $O(10^{-4}) \text{ W kg}^{-1}$ is found within the isothermal doming and leeward side of sill (Figs. 2c,f,i). Clearly, the region above the sill acts as a hotspot of turbulence mixing the high-salinity water advected and raised from the upstream flow with the low-salinity water in the upper layer above the sill. This is a striking example of small-scale processes contributing to sudden changes in larger-scale hydrographic properties. The detailed relationship between turbulent mixing and temperature–salinity (T – S) changes will be discussed in section 5.

b. Flow instability and hydraulic criticality

The upstream and downstream along-transect velocities (v) are mostly 1–2 and 0–0.5 m s^{-1} , respectively, in the upper 100 m (Figs. 3a,e,i). A significant reduction in v occurs 0–4 km downstream from the immediate lee of sill. Above the sill,

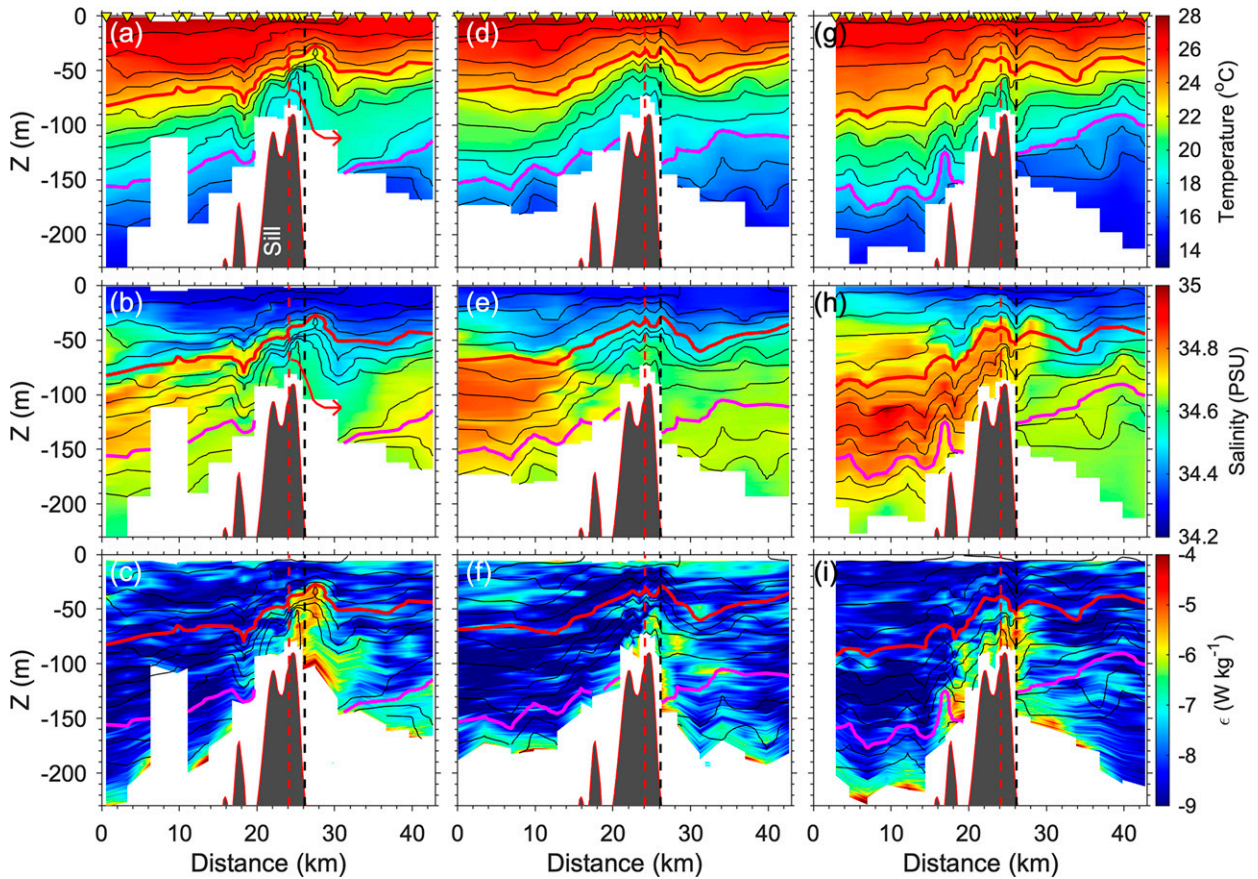


FIG. 2. Distance–depth contours of temperature, salinity, and TKE dissipation rate for (a)–(c) the first transect run, (d)–(f) the second transect run, and (g)–(i) the third transect run in Ex2 (2021). The black contour lines range from 16° to 27°C with an interval of 1°C. The red and magenta lines are the 23° and 18°C isotherms, respectively. The red and black vertical dashed lines denote the locations of G2 and G3, respectively. Locations of VMP profiling are denoted by yellow triangles at the top of (a), (d), and (g). Red arrows in (a) and (b) indicate the possible sources of intermediate water in the lee.

v significantly decreases downward, presumably due to bottom friction. The dramatic change in v in the along-stream direction and in the vertical direction is due to sill (obstacle) obstructing. First, a strong shear squared (S^2) of 10^{-3} s^{-2} is found primarily above sill (Figs. 3b,f,j). The velocity shear squared is computed as $S^2 = (\partial u/\partial z)^2 + (\partial v/\partial z)^2$, where u is the cross-transect velocity. Furthermore, the Richardson number (Ri) is computed as $\text{Ri} = N^2/S^2$, where buoyancy frequency squared $N^2 = -(g/\rho_0)\partial\rho/\partial z$. The occurrence of shear instability is indicated primarily above the sill and in the downstream flow from the sill, where the value of $\text{Ri} < 0.25$ occurs (Figs. 3c,g,k). The strong turbulence (Figs. 2c,f,i) likely results from the shear instability, as they are mostly collocated. Therefore, the shear instability as a result of the bottom boundary shear above the sill explains the isothermal doming. In addition, an intermediate well-mixed layer following the doming can be seen (Figs. 2a,b).

The hydraulic character of the flow (e.g., Farmer and Armi 1999; Armi and Farmer 2002) is examined to link the flow variations to small-scale processes. Typically, this is made by estimating the internal Froude number by assuming a two-layer

flow (i.e., Armi and Farmer 1986; Wesson and Gregg 1994; Moum and Nash 2000). However, the assumption of two-layer flow such that only mode-1 hydraulic character can be examined is not suitable for our observations showing a multimodal hydraulic structure (Fig. 2). Therefore, the better method of determining criticality is to directly estimate the phase speed of the long internal wave modes of the flow, which accounts for continuous variations in both velocity and stratification (Pratt et al. 2000; Gregg and Pratt 2010; Liu et al. 2012; Smyth and Carpenter 2019). The criticality is determined by whether long internal waves can propagate against the flow upstream (subcritical flow) or not (supercritical flow). Implementations for obtaining the internal wave speed are made by solving the Taylor–Goldstein (TG) equation:

$$\frac{d^2\hat{w}}{dz^2} + \left[\frac{N^2}{(U-c)^2} - \frac{1}{(U-c)} \frac{d^2U}{dz^2} - \kappa^2 \right] \hat{w} = 0, \quad (2)$$

where eigenvalue c is the phase speed corresponding to the eigenmode \hat{w} that characterizes the modal structure of vertical velocity, k is wavenumber, and U is the background flow.

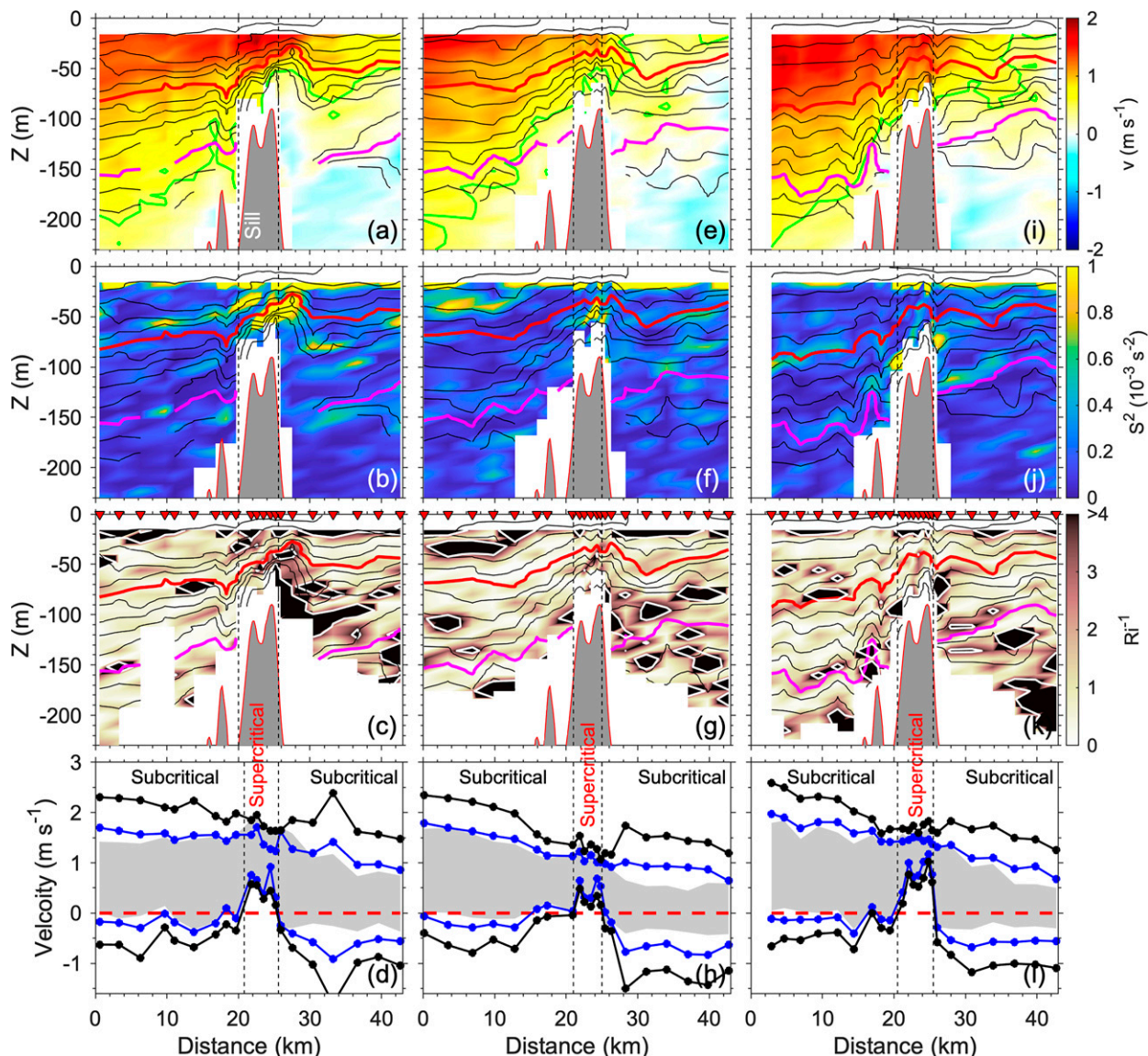


FIG. 3. Distance–depth contours of along-stream velocity v , S^2 , and Ri^{-1} for (a)–(c) the first transect run, (e)–(g) the second transect run, and (i)–(k) the third transect run in Ex2 (2021). Time series of mode-1 (black dots) and mode-2 (blue dots) internal wave propagation speeds for (d) the first transect run, (h) the second transect run, and (l) the third transect run, with gray shading showing the area between minimum and maximum current velocity. The black contour lines range from 16° to 27°C with an interval of 1°C . The red and magenta lines are the 23° and 18°C isotherms, respectively. The black vertical dashed lines denote the locations of criticality transition. The red horizontal dashed lines denote velocity equal to 0 m s^{-1} . Locations of VMP profiling are denoted by red triangles at the top of (c), (g), and (k). The white contour lines in (c), (g), and (k) are $Ri^{-1} = 4$ ($Ri = 0.25$).

The TG equation is solved using the numerical method proposed by Lian et al. (2020). Here, $k = 10^{-6}\text{ m}^{-1}$ is taken to approach the long wave limit (Liu et al. 2012). The buoyancy frequency squared N^2 computed from the VMP hydrographic profiles and the corresponding along-transect velocity measured by the shipboard ADCP are applied to (2). The outcomes include discrete neutral (internal wave) modes, which are our focus, and unstable (growth) modes if $Ri < 0.25$ is reached (Miles 1961; Howard 1961). Essentially, each internal wave mode arises in a pair, with the phase speed in opposite

directions in a U -following frame (Pratt et al. 2000). The phase speeds of the first mode (black dots) and second mode (blue dots) internal waves are shown in Figs. 3d, 3h, and 3l for the three runs, respectively. Mostly, the phase speed pair falls outside the region enclosed by the minimum and maximum of the velocity profile (gray shading) which is in agreement with previous work. An exception occurs for the estimates above the sill due to the simultaneous presence of the unstable mode when $Ri < 0.25$ (Pratt et al. 2000; Liu et al. 2012). The flow above the sill is apparently supercritical (bounded by

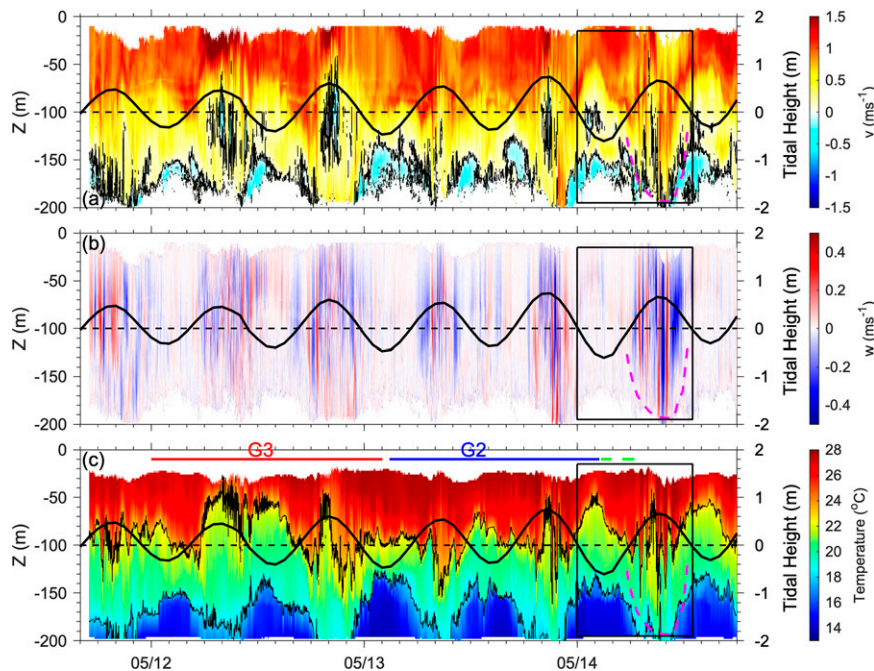


FIG. 4. Time–depth contours of the 1-min average (a) along-stream velocity v , (b) vertical velocity w , and (c) temperature at G3 in Ex1 (2018). The tidal height recorded at the nearby tide gauge station Suao, denoted as a star in Fig. 1a, is superposed in (a)–(c) (thick black lines). The horizontal blue and red lines in (c) denote the time periods of microstructure profiling at G2 and G3, respectively. The two green lines in (c) denote the time periods of the first and second along-track measurements in the 2018 cruise (Ex1). The black contour line in (a) is the 0 m s^{-1} isotach. The two black contour lines in (c) are isotherms at 18° and 23°C .

vertical dashed lines in Fig. 3) because the mode-1 wave pair has identical downstream propagation, whereas the flow upstream and downstream of the sill is subcritical as the mode-1 wave pair propagates in opposite directions. The same occurs to the mode-2 wave. These results suggest that hydraulic control occurs near the northern slope of sill, where the flow transits from supercritical to subcritical conditions. The analyses from the three runs provide a general understanding of the interaction. All three runs are made during low to midtide. Note that the transect surveys are composite (or quasi-synoptic) views of rapidly evolving processes. Inferring and categorizing the evolution from the three runs would be irrelevant since the time needed for each run is ~ 5 h and, as we will unveil, the time scale of the hydraulic transition processes is much shorter than the survey time and the criticality is modulated by tides.

4. Evolution

a. Tidal modulation

During Ex1, mooring G3 was deployed in the immediate lee of sill, located at the downstream edge of the isothermal dome (black dashed line in Fig. 2). The time–depth plot of the moored temperature over a time segment of 3 days mostly shows a three-layer column that is well characterized by the 18° and 23°C isotherms (Fig. 4c). This three-layer structure

could be distorted around the high tide, as we will point out later. By comparing with the first two temperature transects in Ex2, it is well recognized that the top of the isothermal doming separates the upper layer and intermediate layers. The lower interface at ~ 150 m separates the intermediate and lower layers. Strong ϵ mainly occurs in the intermediate layer (Figs. 2c,f), which may lead to well-mixed water in the layer. The water in the layer is likely to originate from the mixed water above the sill via the hydraulic process because T – S properties are similar to those above the sill, which are particularly clear in run 1 (as indicated by red arrows in Figs. 2a,b). The upper, intermediate, and lower layers have along-stream velocity v values of 0.5 – 1.5 , 0 – 0.5 , and <0 m s^{-1} (Fig. 4a). The along-stream velocity and temperature show variability related to sea level height (thick black curve in Fig. 4) varying during a semidiurnal tidal period. Generally, the time series shows that the intermediate layer descends from low tide to high tide, followed by ascending from high tide to the next low tide. Around high tide, the upper bound of the intermediate layer (23°C isotherm) presents a series of high-frequency fluctuations in the range of 50 – 150 m, distorting the three-layer structure. In particular, these high-frequency fluctuations generate strong vertical velocities (w) of ~ 0.1 – 0.4 m s^{-1} (Fig. 4b).

The concurrent 24-h station profiling at G2 on 13 May (measuring period as indicated by the blue line in Fig. 4c) on the sill shows that the along-stream velocity (Fig. 5a) has a

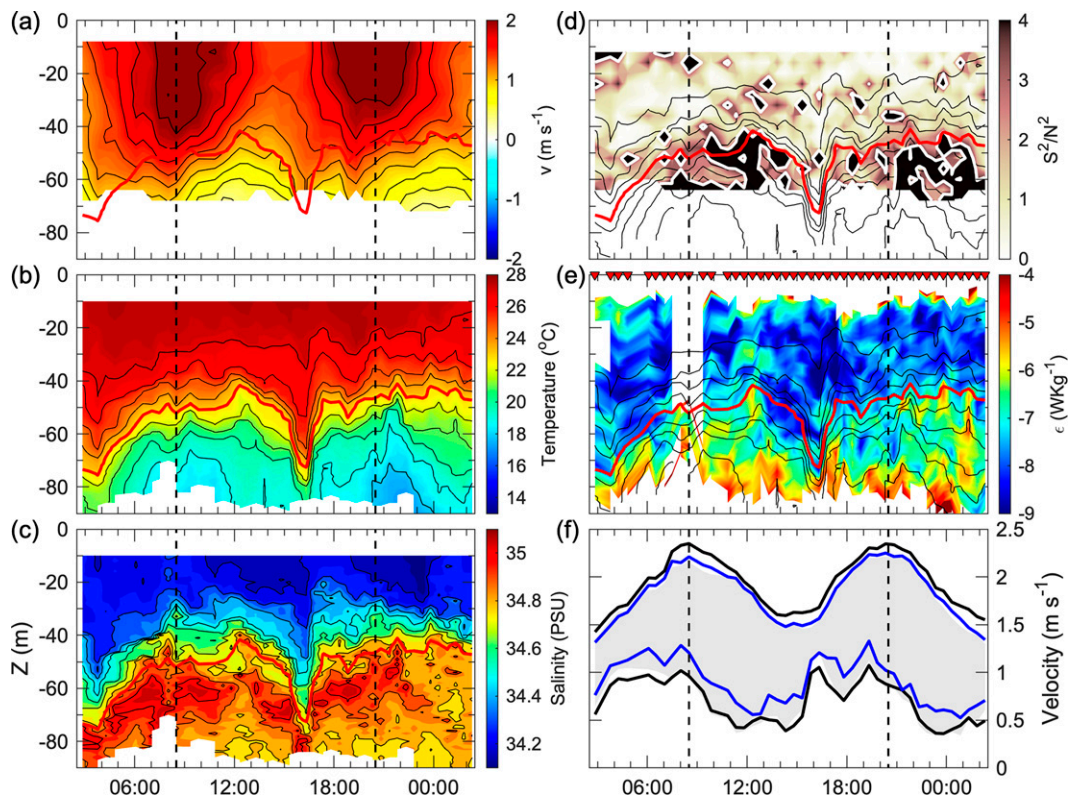


FIG. 5. Time–depth contours of the (a) along-stream velocity v , (b) temperature, (c) salinity, (d) S^2/N^2 , and (e) ϵ by station profiling at G2 and (f) time series of mode-1 (black lines) and mode-2 (blue lines) internal wave propagation speeds in Ex1 (2018). The black contour lines in (a) are the isotachs from 0 to 2 m s^{-1} at an interval of 0.2 m s^{-1} . The black contour lines in (b), (d), and (e) are isotherms ranging from 14° to 28°C with an interval of 1°C . The black contour lines in (c) range from 34.1 to 35.2 psu with an interval of 0.1 psu. The red contour lines are 23°C isotherms. Gray shading in (f) shows the area between minimum and maximum current velocity. The vertical dashed lines denote the time at maximal tidal height.

period of $\sim 12 \text{ h}$ and is highly correlated with tidal height variations. The maximum temperature and salinity differences in the vertical direction can reach 10°C and 1 psu, respectively. Similarly, the top of the isothermal dome is well characterized by the 23°C isotherm (red curves in Fig. 5), which vertically displaces with its maximum amplitude ($\sim 30 \text{ m}$) $\sim 2 \text{ h}$ lagging from the maximum tidal current (Figs. 5a,b). Salinity within the dome has a high value, 34.7–35.1 psu (Fig. 5c), resembling those observed in run 3 in Ex2 (Fig. 2h), showing that the salinity maximum in the upstream flow is carried onto the sill crest. The coexisting regions of $\text{Ri} < 0.25$ (Fig. 5d) and strong ϵ (10^{-7} – $10^{-4} \text{ W kg}^{-1}$; Fig. 5e) within the dome below the 23°C isotherm suggest that the dome forms presumably due to the turbulent mixing resulting from the shear instability above the sill crest. The corresponding variations at G3 are detailed in Fig. 6. The current speed is generally $\sim 0.5 \text{ m s}^{-1}$ weaker than above the sill (Fig. 6a). The intermediate layer is enclosed by 18° and 23°C isotherms (Fig. 6b). Obviously, the water in the upper and intermediate layers here has plunged (30–50 m) from the upper warm water and bottom well-mixed water above the sill, respectively. A clear three-layer structure remains except for the 3-h time segment centered at high tide

(vertical black dashed line in Figs. 5 and 6), when the tidal current above the sill is strongest. Around the high tide, the intermediate layer displaces downward with entrained warm water and numerous small fluctuations from its top. The criterion of shear instability, $\text{Ri} < 0.25$, mostly occurs within the intermediate layer aside from the high tide (Fig. 6d). Around the high tide, the occurrences of shear instability in the intermediate layer are suppressed. The vertical shear is likely weakened due to the occurrences of turbulent mixing as we will demonstrate later that the layer has reached status of marginal instability, i.e., cyclic circumstance in balance between shear forcing and turbulence (Fig. 14b).

b. Unsteady lee waves and KH billows

The transition from the three-layer structure to the mode-1 dominated structure is further revealed by the echo sounder images of two shipboard transects taken from P1 to P2 (Fig. 1b) during the low tide and midtide (two green horizontal lines in Fig. 4c) of a tidal cycle. The mooring data enclosed by the black box in Fig. 4c are included for further analysis. The P1–P2 line is positioned 14.5–27 km from the 45-km full transect. Here, focus is placed on the along-track distance of

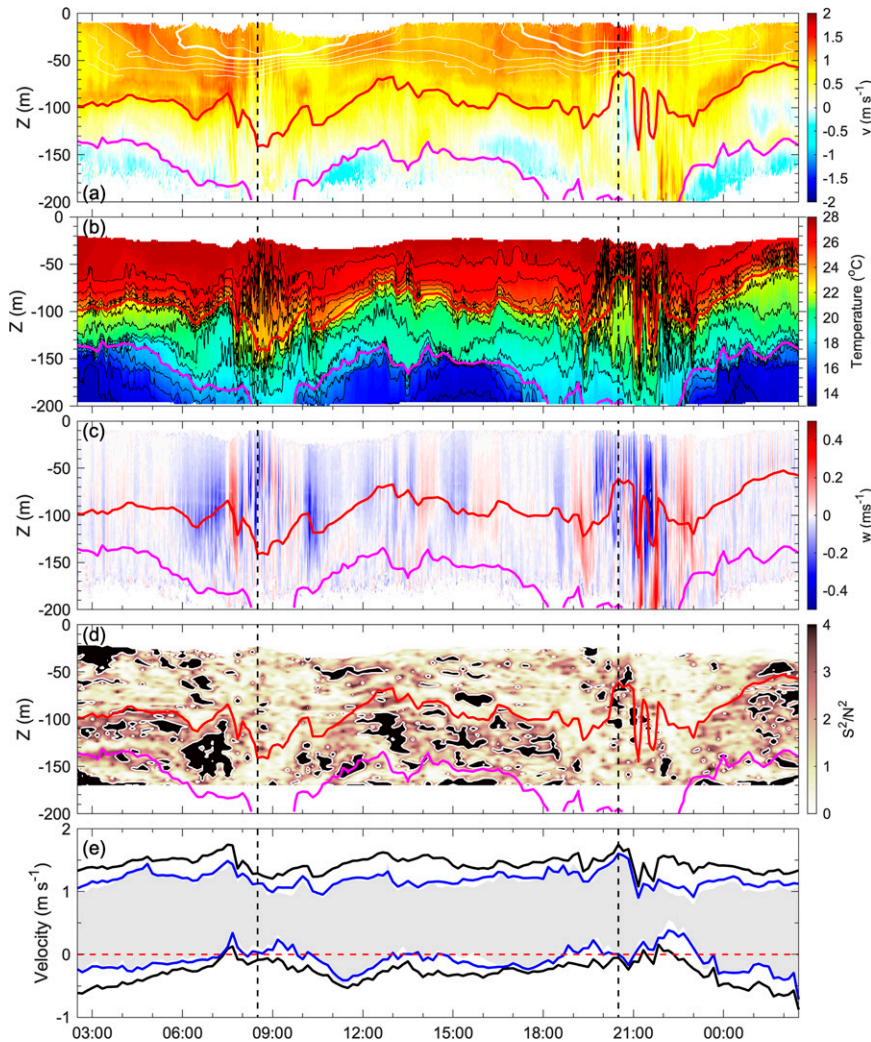


FIG. 6. Time–depth contours of the (a) along-stream velocity v , (b) temperature, (c) vertical velocity, and (d) S^2/N^2 at mooring G3 and (e) time series of mode-1 (black lines) and mode-2 (blue lines) internal wave propagation speeds in Ex1 (2018). The white contour lines in (a) are the isotachs from 1 to 2 m s^{-1} at an interval of 0.2 m s^{-1} at G2. The black contour lines in (b) are isotherms ranging from 14° to 28°C with an interval of 1°C. The red and magenta lines are the 23° and 18°C isotherms, respectively. The vertical dashed lines denote the time at maximal tidal height. The red horizontal dashed lines denote velocity equal to 0 m s^{-1} .

23.5–27 km, where the echo sounder images of the two surveys reveal the rich field of small-scale processes characterized by strong acoustic backscatter bands (Figs. 7a and 8a). During survey 1 (Fig. 7a), a clear train of KH billows, characterized by aligned forward inclination and S-shaped bands (Geyer et al. 2010; Chang et al. 2016), is nearly attached to the crest. This supports the previous conjecture of the occurrences of KH instability using the criterion of $\text{Ri} < 0.25$ (Figs. 3c,g,k, 5d) in Ex2. Lee waves, with a vertical scale of ~ 40 m, are observed at the downstream flank of the sill (indicated by two yellow arrows). Two nearly parallel strong acoustic scattering bands at ~ 60 and ~ 150 m (indicated by two white arrows) are the predominant features on the leeward side of the sill. The strong acoustic backscatter bands

are collocated with the region of strong temperature gradients, suggesting a strong stratification, measured by the mooring as indicated by the vertical black dashed line in Figs. 7b and 7c, when the ship passes through the G3 mooring at 0244 UTC. Noticeably, the strong stratification is mostly accompanied by strong shear. An intermediate layer is sandwiched by the two bands of strong stratification/shear (Figs. 7b,d). Hereafter, the bands are termed the free shear layer (FSL). The upper FSL lowers slightly at 0305 UTC, followed by a successive plunge of warm water in conjunction with small undulations initiating at approximately 0430 UTC (highlighted by the red arrow in Fig. 7b), while the strong flow in the upper layer begins to separate, forming a jet-like flow at approximately 80–100 m. The FSL collocated with the jet flow in the upper periphery of the

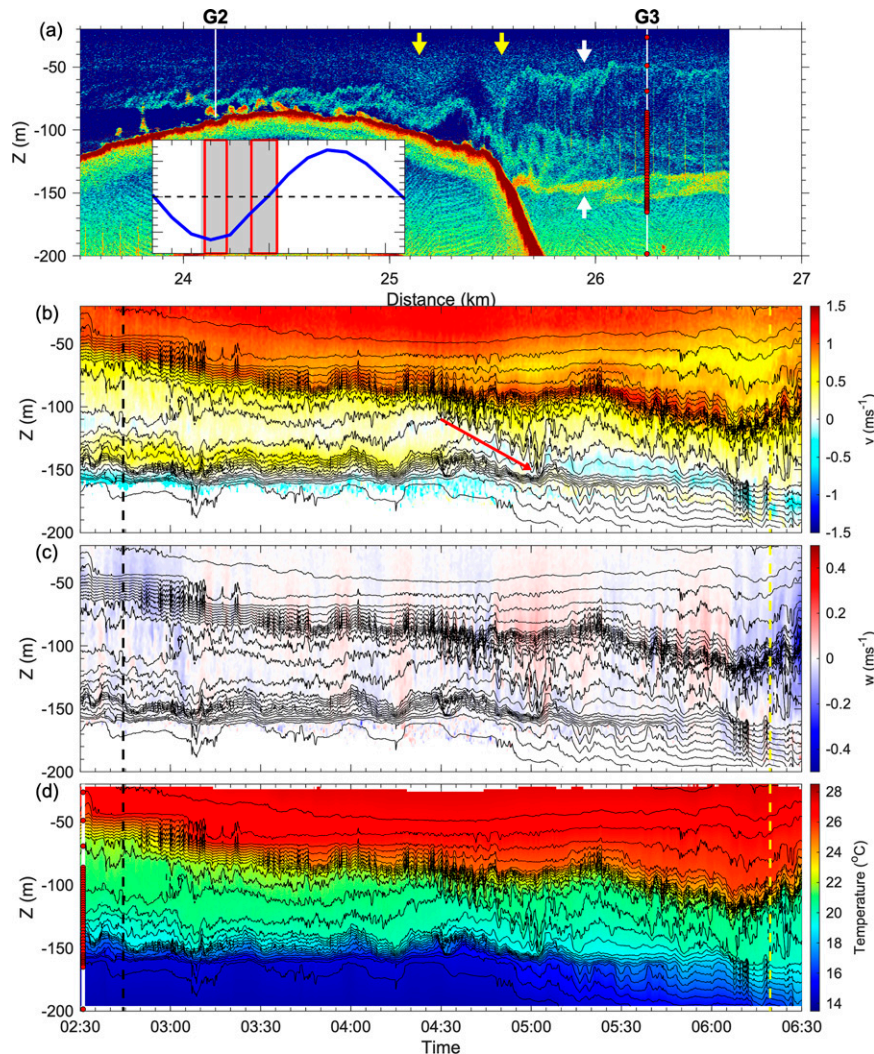


FIG. 7. (a) Echo sounder image taken during survey 1 in Ex1 (2018). Time–depth contours of (b) along-stream velocity, (c) vertical velocity, and (d) temperature measured by mooring G3. The contour lines in (b)–(d) show that the thermal variations range from 14° to 28°C with an interval of 0.5°C. The vertical white lines in (a) denote the positions of stations G2 and G3. The red dots in (a) and (d) are the locations of the temperature sensors. The black and yellow dashed lines in (b)–(d) mark the time point when the ship passed through mooring G3 for the first and second surveys, respectively. The inset shows the time series of the tidal height, with gray shading showing the time segment of (b)–(d) and with two red boxes showing the durations of surveys 1 and 2.

intermediate layer becomes wavy from 0530 to 0730 UTC (Figs. 7b and 8b). This can be thoroughly explained by combining the echo sounder images taken during survey 2 (Fig. 8a).

In survey 2, the preceding lee waves observed in survey 1 are advected downstream, with additional lee waves forming close to the sill, numbered from 1 to 4 in Fig. 8a. The ship surveys from the sill to the lee of the sill and passes through mooring G3 at 0619 UTC (denoted as a vertical yellow dashed line in Figs. 7b–d). As indicated by previous studies (Winters 2016; Musgrave et al. 2016), the structure of the lee wave consists of an upwelling region and a downwelling region in the

front (downstream) and trailing (upstream) edges, respectively. Indeed, a downward velocity of $w = -0.2 \text{ m s}^{-1}$ is measured by the moored ADCP during approximately the period that the ship passes G3 (vertical yellow dashed line in Fig. 7c), while the mooring is at the trailing edge of lee wave 3 (Fig. 8a). It is clear that lee wave 2 is advected downstream due to the acceleration of tidal currents from low to midtide and is then captured by the mooring at 0655–0725 UTC. Evidence includes 1) the strong backscatter revealing the trough of lee wave 2 (highlighted by the upper blue dashed line in Fig. 8a) correlating well with the strong temperature gradient at 120–130 m

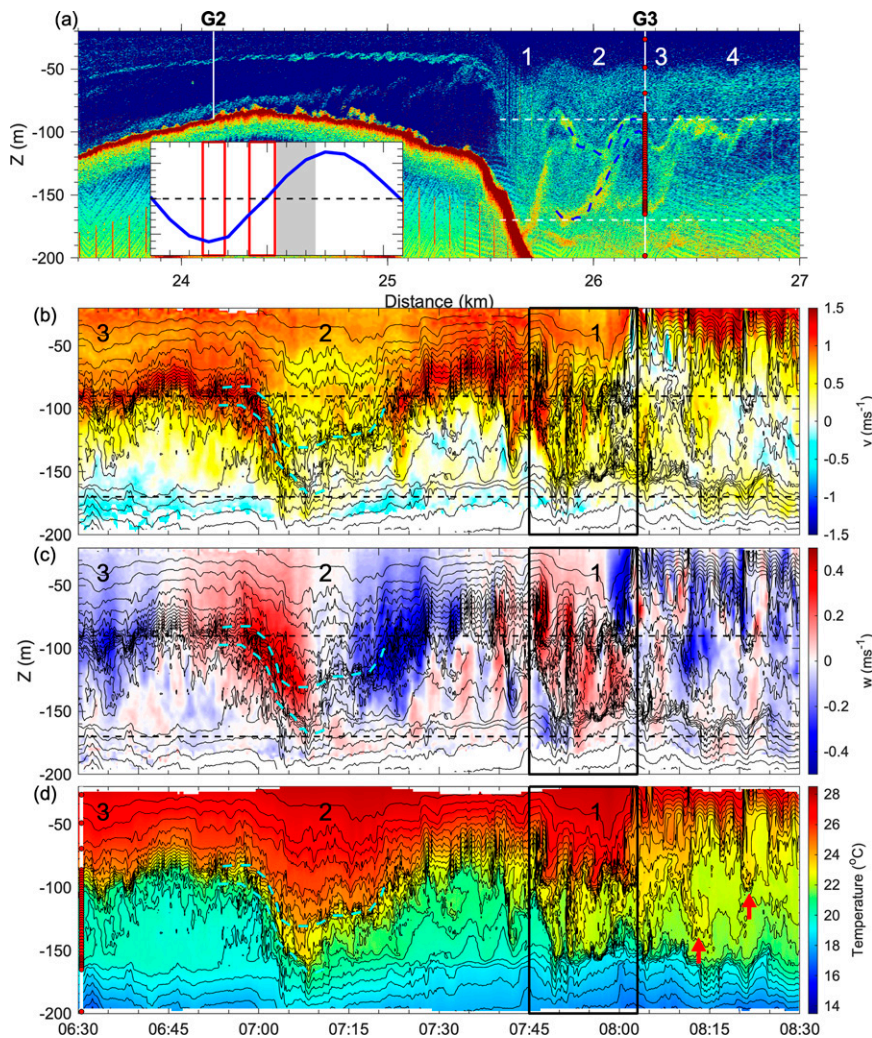


FIG. 8. (a) Echo sounder image taken during survey 2 in Ex1 (2018). Contour plots of (b) along-stream velocity, (c) vertical velocity, and (d) temperature measured by mooring G3. The contour lines in (b)–(d) show that the thermal variations range from 14° to 28°C with an interval of 0.5°C. The vertical white lines in (a) denote the position of station G3. The red dots in (a) and (d) are the locations of the temperature sensors. The inset shows the time series of the tidal level, with gray shading showing the time segment of (b)–(d) and with two red boxes showing the durations of surveys 1 and 2. The two horizontal dashed lines in (a)–(c) denote depths of 90 and 170 m.

(highlighted by the upper cyan dashed line in Fig. 8b) and 2) a clear pair of upwelling and downwelling ($\sim 0.4 \text{ m s}^{-1}$; Fig. 8c) is related to the front and trailing edges of lee wave 2 (Fig. 8d). It is noted that the strong jet mentioned previously is depressed and then elevated, i.e., nearly flowing along the trough of the wave (Fig. 8b).

Another significant feature captured by the echo sounder is the S-shaped acoustic scattering bands below the lee waves (Fig. 8a). These S-shaped acoustic backscatter bands resemble the manifestation of KH billows (Geyer et al. 2010; Chang et al. 2016). The moored observations lend further support to the process. The S-shaped acoustic scattering band below lee wave 2 (highlighted by the lower blue dashed line in Fig. 8a)

corresponds to the downward plunging of the strong temperature gradient (lower cyan dashed lines in Figs. 8b–d). Note that both the lee wave and S-shaped acoustic backscatter band captured by the echo sounder are flipped in the time–depth contour of the mooring measurement because the front side of the features are measured earlier and vice versa. Indeed, the contour of thermal variation (Fig. 8d) shows a roll-up of temperature at 0705–0710 UTC, which suggests a KH billow growing at the front trough of lee wave 2. It is likely that the KH billow grows at the expense of the kinetic energy of the jet flow at the lower periphery of the wave.

The following wave marked by 1 in Figs. 8b–d is expected to be lee wave 1, as shown in Fig. 8a. Lee waves 1 and 2

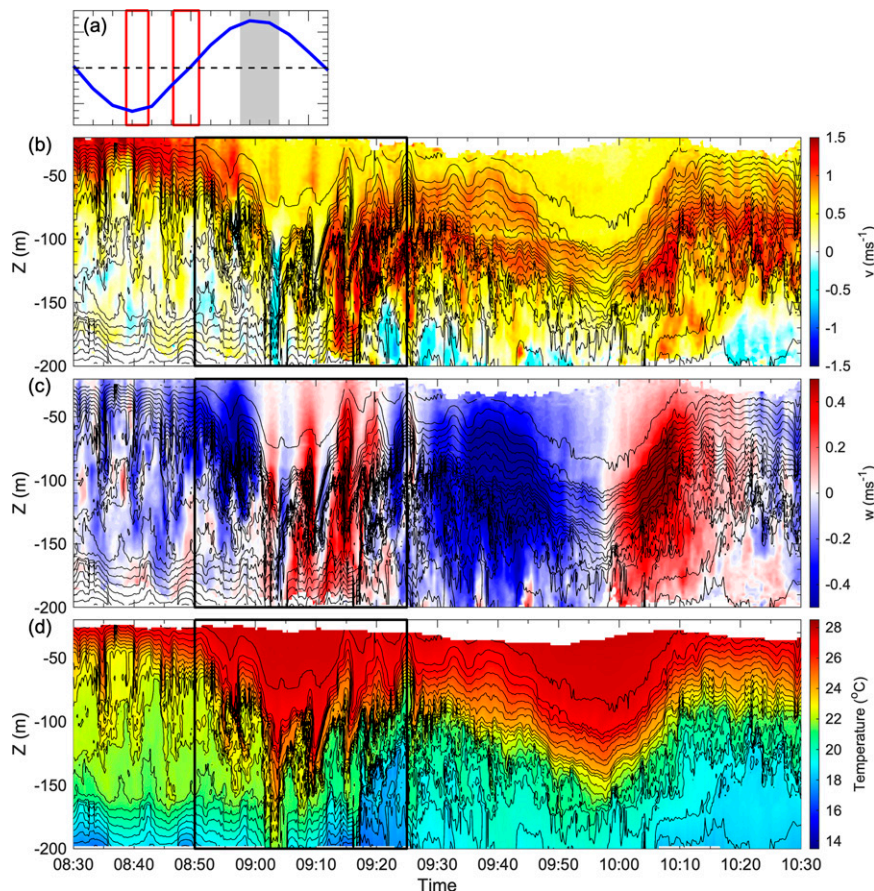


FIG. 9. (a) Time series of the tidal level. Contour plots of (b) along-stream velocity, (c) vertical velocity, and (d) temperature measured by mooring G3. The contour lines in (b)–(d) show that the thermal variations range from 14° to 28°C with an interval of 0.5°C. The gray shading in the inset shows the time segment of (b)–(d). The two red boxes in the inset show the durations of surveys 1 and 2.

revealed by the echo sounder image have similar structures. However, there is no clear correspondence between the echo sounder image and the moored measurement for lee wave 1 (0745–0800 UTC). The measurements of the moored thermistor chain show that lee wave 1 has a breaking waveform, characterized by a chaotic thermal patch and numerous billow-like rollups at 50–170 m (Fig. 8d). Presumably, the breaking waveform results from the collapse in KH instability. Hereafter (0800–0850 UTC), the upper warm layer with strong flow is upwelled to above 50 m, and the intermediate layer becomes thicker (~100 m) but is ~3°C warmer (Figs. 8d and 9d), likely due to entrainment and turbulent mixing with the upper warm layer. Meanwhile, the roll-up structure as a result of KH instability is frequently observed in this stage, which is approximately the period of high tide. Two clear examples of roll-up are indicated by two arrows in Fig. 8d. Just after the highest tidal level (0850 UTC), implying the beginning of tidal flow deceleration, lee wave 1 returns to the G3 mooring, as revealed by the contour plot at 0850–0925 UTC (enclosed by black boxes in Figs. 9b–d), showing the nearly mirrored structure of that previously measured at 0745–0803 UTC (enclosed

by black boxes in Figs. 8b–d). Lee wave 1 captured at 0745–0803 UTC has a series of three patches of strong positive w (Fig. 5c) that gently lower, followed by a strong negative w at 20–90 m. The strong positive velocity is located near the upward rolling side of the billows. In contrast, the features are flipped in the time axis during the second measurement (Fig. 9c), i.e., the strong negative w in the upper layer (0850–0900 UTC) is followed by a series of three patches of strong positive w (0900–0925 UTC), two of which have their negative counterpart that is absent in the first measurement. The structure of KH billows becomes well defined, whereas they are unclear in the first measurement. The subsequent wave at 0930–1010 UTC is likely the returned lee wave 2, showing the flipped w in the time axis as earlier observed downwelling followed by upwelling due to its upstream movement. The previously observed billows disappear here. Both returned waves have longer time scales, possibly due to the varied translating speed, and the vertical scale and w becoming stronger. Subsequently, the processes return to the predominance of the intermediate well-mixed layer.

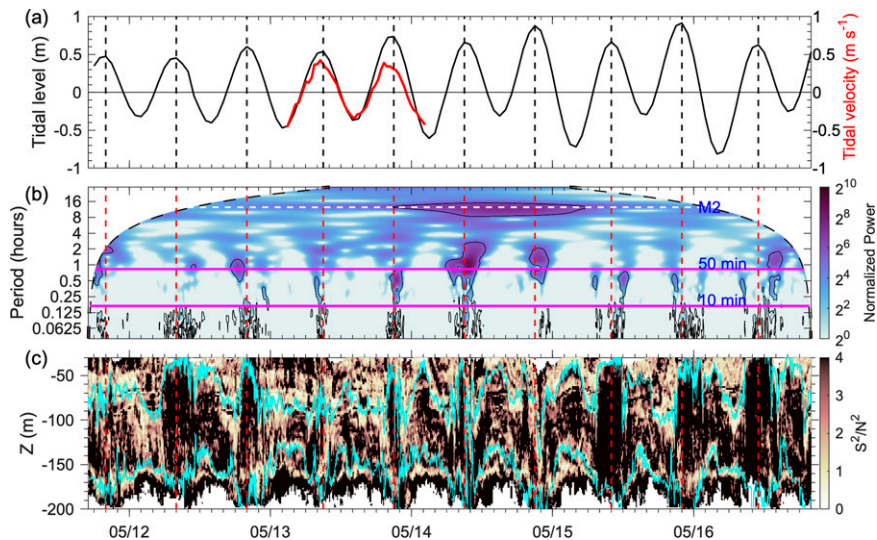


FIG. 10. (a) Time series of the tidal height at Suao (black line) and tidal velocity at G2 (red line). (b) The wavelet power spectrum for vertical velocity averaged over 50–150 m at G3. Time–depth contours of the (c) S^2/N^2 at mooring G3. The black contours in (b) enclose the regions of confidence level larger than 95%. The vertical dashed lines denote the time of maximum tidal level. The cyan contour lines in (c) are the 19° and 25°C isotherms.

c. Interpretation

The driving mechanisms leading to the evolution shown in Figs. 7–9 can be interpreted by the transition of the hydraulic character as a result of the tidal flow modulation. Returning to the simultaneous observations at G2 (Fig. 5) and G3 (Fig. 6), the flow is clearly supercritical with respect to both mode-1 and mode-2 waves above the sill at G2 (Fig. 5f) as their wave pairs propagate downstream throughout the two tidal periods, although the wave speeds determined using the TG equation are strongly modulated by the tide. However, the criticality at G3 is varied (Fig. 6e). At G3, with respect to the mode-1 wave, the flow is mostly subcritical. In contrast, with respect to the mode-2 wave, the flow is mainly supercritical around the high tide but is subcritical in the low and midtides. This suggests the presence of a mode-1 and a mode-2 critical control section between G2 and G3 or adjacent to G3 during the period of low and midtides. Specifically, the mode-1 and mode-2 perturbations could be arrested and accumulate between G2 and G3. The (mode-1) lee waves and the three-layer structure, i.e., the intermediate layer, likely result from the accumulation of the mode-1 and mode-2 perturbations, respectively (Figs. 7a and 8a). Lee wave formation as a result of flow criticality was demonstrated by Xie and Li (2019). Around the high tide, the tidal flow is strengthened so that the lee waves are advected downstream and only the mode-1 critical control section could occur between G2 and G3, resulting in the mode-1 warm-water depression/entrainment (0800–0850 UTC in Figs. 8d and 9d), accompanied by strong flow ranging only in the upper 50 m. The presence of the strong flow suggests that the flow above the sill is extended further leeward at G3, leading to the supercriticality of mode-2 waves at G3. The signals of upper strong flow are well-identified

in the 3-day time series during high tide (Fig. 4). The above processes repeatedly occur in each tidal cycle in our measuring period.

We further elucidate the tidal modulation using the 5-day moored measurements (Fig. 10). The along-stream tidal velocity (red curve in Fig. 10a) above the sill, obtained from the depth-averaged and demeaned 24-h shipboard ADCP measurements (Fig. 5a), is well correlated with the tidal height at Suao (black curve in Fig. 10a). Thus, tidal height is a relevant indicator of tidal flow magnitude above the sill. The wavelet analysis of vertical velocity (Fig. 10b) shows a band of high wavelet power centered on the M₂ tidal period. Moreover, the significant wavelet power regions roughly centered on 50 min and shorter than 10 min, as enclosed by a 95% confidence level, are related to the unsteady lee waves and KH instabilities, respectively, which occur predominantly around the high tide. The simultaneous occurrences of lee wave and shear instability signatures (Fig. 10b) suggest instability growing along with the lee wave, as shown in Fig. 9d. The criterion of shear instability, $Ri < 0.25$, occurs more intensively around the high tide (Fig. 10c), which lends further support. Overall, the wavelet spectra reveal a downscale energy cascade from Kuroshio flow to lee waves and shear instabilities, both modulated by the tidal flow. The next section will present the subsequent downscale cascade to turbulent mixing.

5. Turbulent mixing

a. Statistics

The microstructure profiles were taken in two tidal cycles (Fig. 11c), as denoted by the red line in Fig. 4c. The ship heads slightly against the current during the station profiling to

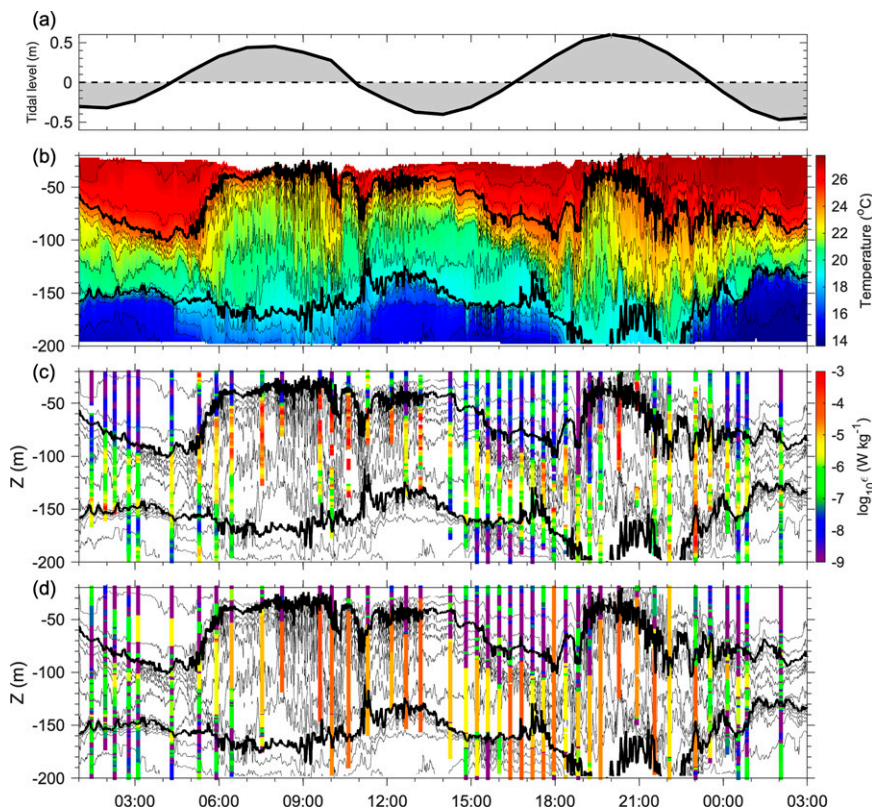


FIG. 11. (a) Time series of the tidal height at Suao. (b) Contour plot of 1-min average temperature at mooring G3. (c) Time–depth plot of TKE dissipation rate from (c) shear probe measurements (ϵ) and (d) estimate of Thorpe scale method based on the VMP hydrographic data (ϵ_{VH}). The contour lines in (b)–(d) show that the thermal variations range from 14° to 28°C with an interval of 1°C. The thick contour lines in (b)–(d) are the 19° and 25°C isotherms.

ensure the VMP-500 is slackly tethered and freely sinks. The ship could occasionally run against the current around the high tide phase, leading to a low falling rate and tilting of VMP-500 and resultant poor data quality. Therefore, we omit the data sampled at tilting angle $> 10^\circ$ or falling rate $< 0.2 \text{ m s}^{-1}$ (Douglas and Lueck 2015); this results in the missing data around high tide (Fig. 11c). In addition, ϵ at $O(10^{-3}) \text{ W kg}^{-1}$ is excluded from our analysis because the angles of attack of shear probe could be larger than 20° (see the appendix). TKE dissipation rate estimated using Thorpe scale method (Thorpe 1977; Dillon 1982; Galbraith and Kelley 1996) based on VMP hydrographic data (ϵ_{VH} ; Fig. 11d) shows consistent variations with shear probe measurements (ϵ). Though ϵ_{VH} has a relatively low vertical resolution, the time series of depth-averaged $\log_{10}\epsilon_{VH}$ nearly coincides with that of $\log_{10}\epsilon$. The comparison results give confidence to the microstructure observations.

The strong TKE dissipation rate mostly occurred in the depth range enclosed by the 19° and 25°C isotherms (Figs. 11b–d), which approximately characterized the intermediate well-mixed layer at approximately low and midtides (Fig. 11a). Similarly, ϵ was also modulated by the tide. Around low tide, ϵ was mostly $O(10^{-7}\text{--}10^{-5}) \text{ W kg}^{-1}$ and became stronger around midtide [$O(10^{-6}\text{--}10^{-4}) \text{ W kg}^{-1}$]. Around high tide, the strongest ϵ ,

$O(10^{-4}) \text{ W kg}^{-1}$, occurred. The measured ϵ ranged from 10^{-10} to $10^{-4} \text{ W kg}^{-1}$. The value of the most frequent occurrence was $O(10^{-6}\text{--}10^{-7}) \text{ W kg}^{-1}$, which accounted for 48% of the occurrence. Eddy diffusivity was estimated using $K_\rho = \Gamma \epsilon N^{-2}$ (Osborn 1980), where $\Gamma = 0.2$ is the mixing efficiency. The water properties of the Kuroshio east of Taiwan are highly diverse regarding the significant discrepancy in temperature–salinity relationships reported in Mensah et al. (2014). They further estimated that a value of $K_\rho \sim O(10^{-3}) \text{ m}^2 \text{ s}^{-1}$ was needed to mix the water masses, which was likely a result of flow influenced by local topography. Our measured K_ρ was concentrated on a range of high values, from $O(10^{-4})$ to $O(10^{-3}) \text{ m}^2 \text{ s}^{-1}$. Chang et al. (2013) and Chang et al. (2016) reported hotspots of strong flow–topographic interactions on the leeward side of Green Island and a seamount sitting in the main path of the Kuroshio, respectively. Our microstructure measurements suggest an additional hotspot—the I-Lan ridge, revealing that 36% of the K_ρ was larger than the regional mean value of $10^{-3} \text{ m}^2 \text{ s}^{-1}$ proposed by Mensah et al. (2014).

b. Impacts on water masses

As shown in Fig. 2, the 45-km transect exhibited strong discrepancies in T – S properties. The role of turbulent mixing on the variability of water mass properties was examined. The

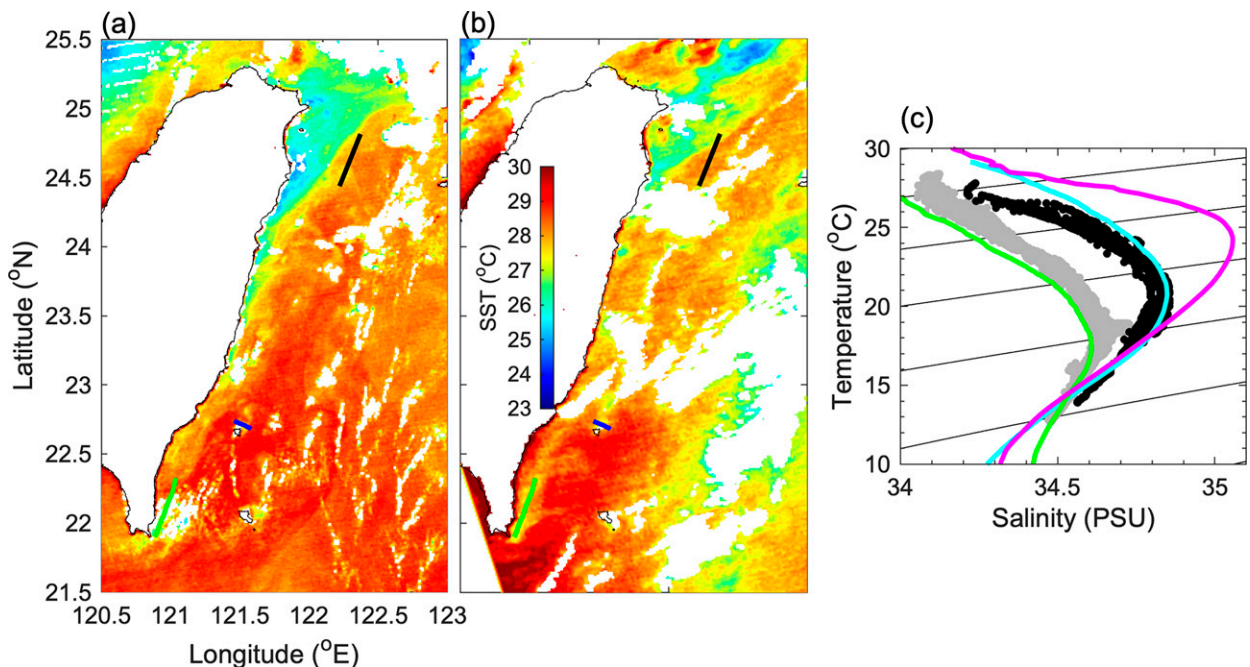


FIG. 12. *Aqua*/MODIS SST taken at (a) 0500 UTC 15 May 2021 and (b) 0430 UTC 12 May 2021. (c) T - S diagram observed on the leeward side of Green Island (black dots) and off the southeastern coast of Taiwan (gray dots). The thick black, blue, and green lines in (a) and (b) are the hydrographic transects around the sill (same as Fig. 1b), on the leeward side of Green Island and off the southeastern coast of Taiwan, respectively. The magenta, cyan, and green curves are the averaged T - S curves for Kuroshio water east of Luzon Island, West Philippines Sea Tropical Water (WPSTW), and South China Sea Tropical Water (SCSTW), respectively (Jan et al. 2015).

2021 cruise (Ex2) was conducted during 10–17 May. Transect surveys (black line in Figs. 12a,b) around the sill on the I-Lan Ridge were performed during the first three days. Another two upstream transects on the leeward side of Green Island (blue line) and off the southern tip of Taiwan (red line) were performed after the I-Lan Ridge surveys. Satellite sea surface temperature (SST) on 15 May (Fig. 12a) revealed that the transect at Green Island (blue line) had a warm SST due to Kuroshio warm water, whereas the onshore side southeast of Taiwan (red line) had a 1°C colder SST. The onshore cold water became more significant and was likely attached with the onshore flank of the Kuroshio, forming a front adjacent and parallel to our transect on the I-Lan Ridge (black line in Fig. 12a). Hydrographic measurements along the Green Island transect show T - S properties of the water mass (black dots in Fig. 12c) were close to (cyan curve in Fig. 12c) those of the WPSTW (Jan et al. 2015; Mensah et al. 2014), which is the typical water mass in the Kuroshio east of Taiwan. In contrast, hydrographic measurements off southeastern Taiwan show T - S properties (gray dots in Fig. 12c) resembling those of the South China Sea Tropical Water (SCSTW; green curve in Fig. 12c), which has been frequently found along the onshore flank of the Kuroshio (Chen 2005). The front passed through our transect on 12 May during our sill survey (Fig. 12b), with cold and warm SSTs in the northern and southern parts of the transect, respectively.

The cold SST was an indicator of SCSTW because the water mass property of SCSTW was distinct north of the

transect (Figs. 13a,c,e). WPSTW became noticeable south of the transect. However, the two water masses lost their identity, as T - S properties were mostly scattered between the characteristic T - S curves of WPSTW and SCSTW, particularly in the middle of the transect, where the sill is located. Strong mixing frequently occurs in regard to T - S properties scattered between the two masses (Figs. 13b,d,f), which provides further verification. It should be noted that the sources of SCSTW could also originate from the Taiwan Strait throughflow in northern Taiwan, as indicated by Jan et al. (2006), except for that originating from the onshore side of the Kuroshio. Since the WPSTW–SCSTW front is persistently present adjacent to the sill (Jan et al. 2013), the region of the sill transect is a hotspot eliciting mixing between two water masses initiated by the hydraulic transition, as was evident in our observations.

c. Mechanisms leading to turbulent mixing

Shear instability was demonstrated to occur in the bottom boundary layer above the sill and in the immediate lee where the hydraulic transition is predominant using the criterion $Ri < 0.25$ (Figs. 3c,g,k, 5d, 6d, and 10c). These billows were directly observed above the sill (Fig. 7a), in the lee waves (Figs. 8a,d and 9d), and within the warm depression (Fig. 8d). KH billows appeared in the free shear layer as well (Fig. 14a). Therefore, the shear instability seems to act as the final piece to transform the flow kinetic energy to turbulence via the hydraulic transition that spawns the intermediate layer sandwiched by

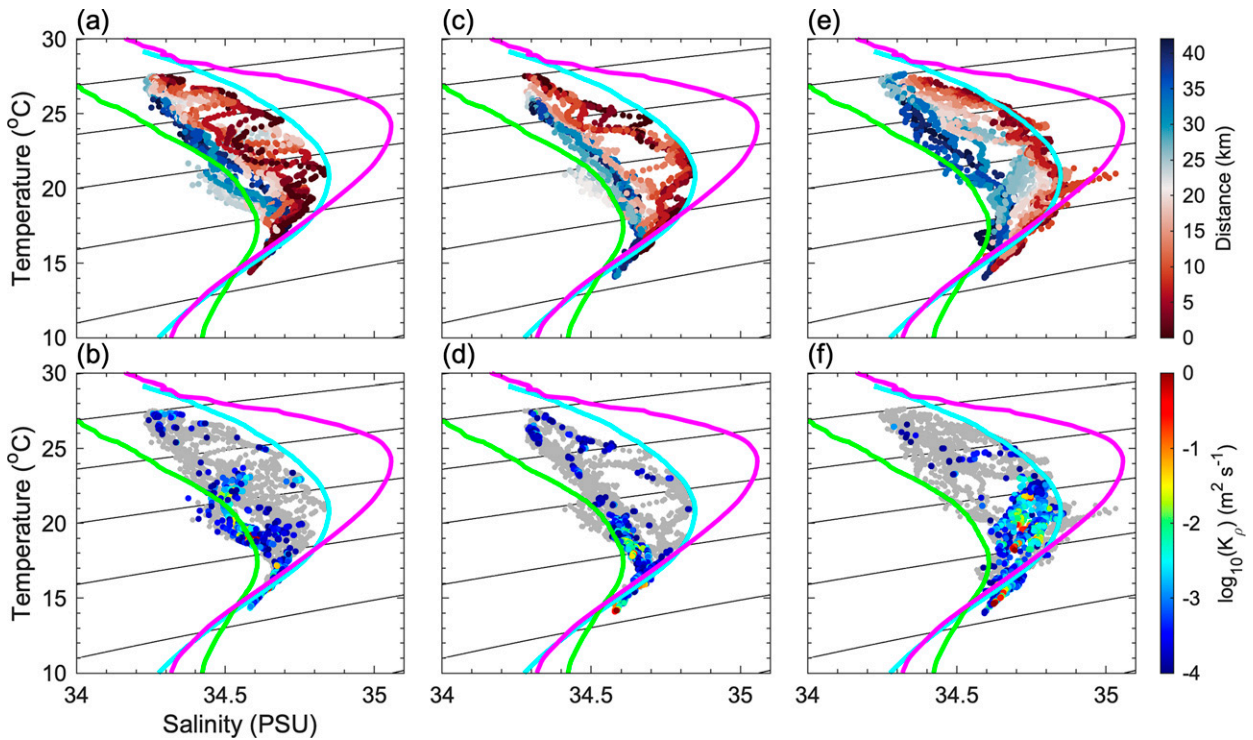


FIG. 13. T - S diagram observed in the (a),(b) first transect run, (c),(d) second transect run, and (e),(f) third transect run. Dot colors in (a), (c), and (e) represent the transect distance. Dot colors in (b), (d), and (f) represent $\log_{10}K_p$, which is gray shaded if $\log_{10}K_p < -4$. The magenta, cyan and green curves are the averaged T - S curves for Kuroshio water east of Luzon Island, WPSTW and SCSTW, respectively (Jan et al. 2015).

two free shear layers, the lee waves, and the warm depression. On the whole, this can be further summarized by the probability density function (PDF) of Ri estimated using the 5-day time series of current and temperature measurements at 50–180 m, where the above small-scale processes result in the hydraulic transition (Fig. 14b). The distribution of Ri fluctuates at a center

value near 0.25, which is a key feature of marginal instability status (Thorpe and Liu 2009; Smyth 2020; Chang 2021). This can be interpreted as a cyclic circumstance in balance between shear forcing and turbulence. The small-scale processes based on the hydraulic transition progressively strengthen shear such that the flow reaches the condition of shear instability

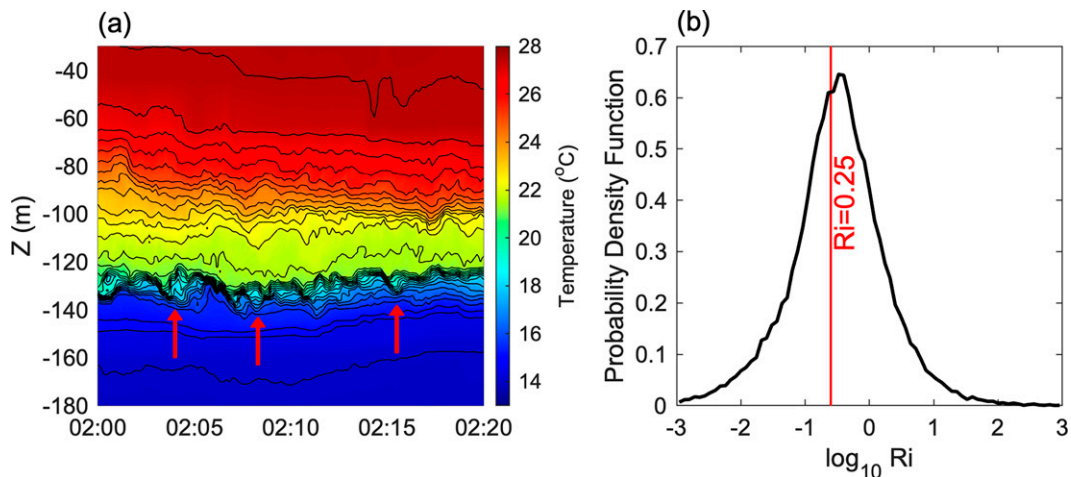


FIG. 14. (a) Time–depth contour of temperature at G3 from 0200 to 0220 UTC 13 May 2018 and (b) probability density function of $\log_{10}(Ri)$ estimated using the mooring data at G3. The three arrows point out three examples of KH billow.

$Ri < 0.25$. Consequently, turbulent mixing as a result of the collapse of shear instability reduces the shear. Ri then increases restoring the stability. Eventually, the probability distribution of Ri concentrates at a value near 0.25. The results suggest that the shear instability plays a crucial role in the turbulent transition. The marginal instability above the sill boundary layer is likely. However, it is difficult to verify because the near-bottom current is measured poorly by the shipboard ADCP. Furthermore, there may be other processes leading to turbulence. The convective instability due to warm water downwelling and the distortion of leeward waves forced by advection could be the secondary factor responsible for the turbulent transition. Finally, the frontal area may favor the occurrences of the interleaving process, as found by Jan et al. (2019). Indeed, interleaving, indicated by the zigzag-like T - S distribution, can be observed in the T - S diagrams (Figs. 13a,c,e). The convective instability and interleaving merit a further study.

6. Discussion and conclusions

Understanding the turbulent mixing driven by stratified flow over topography requires the observational examination of internal hydraulic flows and lee waves (Legg 2021). Previous observations were mostly made over either tidal flow-dominated sills or subinertial flow-dominated (abyssal) seamounts, whereas their combining effects were rarely observed. A detailed review was provided in Legg (2021). Lee waves (Klymak et al. 2008; St. Laurent et al. 2012; Alford et al. 2014) and internal hydraulic flows (Farmer and Armi 1999; Wesson and Gregg 1994; Moun and Nash 2000; Nash and Moun 2001; Armi and Farmer 2002; Klymak and Gregg 2004; Alford et al. 2013) were individually observed in these studies though they could coexist. As an exception, Musgrave et al. (2016) reported the advection of a breaking tidal lee wave that extends from the ridge crest to the surface and the subsequent development of a hydraulic jump on the ridge's flanks. Tanaka et al. (2021) reported an internal hydraulic jump when the flow passes over an abrupt sill. The echo sounder captured 50-m-tall lee wave-like fluctuations, which were not further interpreted. In addition, the observed hydraulic flows were predominantly mode-1 control so that the internal Froude number based on two-layer flow was capable of determining the hydraulic character (Wesson and Gregg 1994; Moun and Nash 2000). Gregg and Klymak (2014) reported a hydraulic control of mode-2 lasting more than 3 h over a continental shelf, corresponding to a TKE dissipation rate from 10^{-8} to 10^{-7} $W\ kg^{-1}$. Our observations detail the downscale cascade processes of flow-topography interactions based on subinertial flow modulated by the tides that comprise mode-1 and mode-2 internal hydraulic flows, unsteady lee waves, shear instability, and vigorous turbulent mixing.

Here, we present observations of complex small-scale processes and energetic turbulence above a sill located at the I-Lan Ridge that spans across the strong Kuroshio. Multiple platform measurements include a fast-sampling and high-resolution moored thermistor chain and ADCP, shipboard echo sounder, and turbulence profiler. The flow above the sill is strong ($1.5\ m\ s^{-1}$) and unsteady ($\pm 0.5\ m\ s^{-1}$) due to the Kuroshio flow, which is periodically modified by the semidiurnal tidal

current. In other words, the flow speed oscillates with a large amplitude but has a consistent flowing direction because of the strong mean flow, suggesting that tidally induced flow reversal does not exist. Therefore, these processes are mainly driven by geostrophic flow in which the flow magnitude is significantly modulated by the tidal current.

Our observations demonstrate the encountering of the strongly unsteady flow with the sill leads to the generation of a rich field of small-scale processes, fast evolution, and intense turbulent mixing that changes over time, which have rarely been addressed before. Above the sill, isothermal domes are possibly generated by turbulent mixing as a result of shear instability occurring in the bottom boundary layer. The vertical scale of isothermal domes ranges from 20 to 50 m and is modulated by tidal flow. Alternatively, flow advection could play a role. One of our three cross-sill sections shows the upstream flow could climb on the sill crest as the salinity maximum at ~ 100 – 200 m observed in the upstream rises to 50–100 m above the sill crest (Fig. 2h), which is, however, absent in the other two sections (Figs. 2b,e). Stratification could restrict vertical displacements, driving the flow to pass around rather than over the sill; this is examined by Burger number $Bu = [Nh_0/(fL)]^2$, where f and L are Coriolis parameter and horizontal scale of the sill, respectively. The average $N \sim 0.012\ s^{-1}$ in the upstream is nearly consistent in the three transects. Bu is ~ 140 , much larger than 1, given $h_0 \sim 300$ m, $f \sim 6 \times 10^{-5}\ s^{-1}$, and $L \sim 5$ km. This suggests flow is mostly influenced by stratification (Cushman-Roisin and Beckers 2011), pointing out turbulent mixing plays a more important role in shaping the isothermal dome. High Bu also suggests the occurrence of lateral shear layer and eddies in the lee of the sill, which is ignored in this study.

Observations suggest that the small-scale processes on the leeward side of the sill are initiated by the tidally modulated hydraulic character. The criticality determined by the TG equation shows that the flow is supercritical with respect to both mode-1 and mode-2 waves above the sill over the whole tidal phase. In contrast, the criticality in the immediate leeward side has a dependence on the tidal phase. The flow is mostly subcritical with respect to the mode-1 wave throughout the tidal phase. However, the mode-2 wave has a slower phase speed, which is sensitive to the strong background flow. With respect to the mode-2 wave, the flow is subcritical in the low and midtides but is supercritical around the high tide. This suggests the presence of a mode-1 and a mode-2 critical control section between the sill crest and the immediate lee during the period of low and midtides. As a result, both the mode-1 and mode-2 perturbations are expected to accumulate. The mode-1 lee waves and the three-layer structure, i.e., the intermediate layer, likely develop from the accumulation of the mode-1 and mode-2 perturbations, respectively. Around the high tide, the lee waves are advected further downstream, and only the mode-1 critical control section occurs such that the hydraulic transition forms the mode-1 warm water depression. The above processes repeatedly occurred in each of the tidal cycles in our measuring period.

Shear instability serves as the final piece transforming the flow kinetic energy to turbulence via the above hydraulic

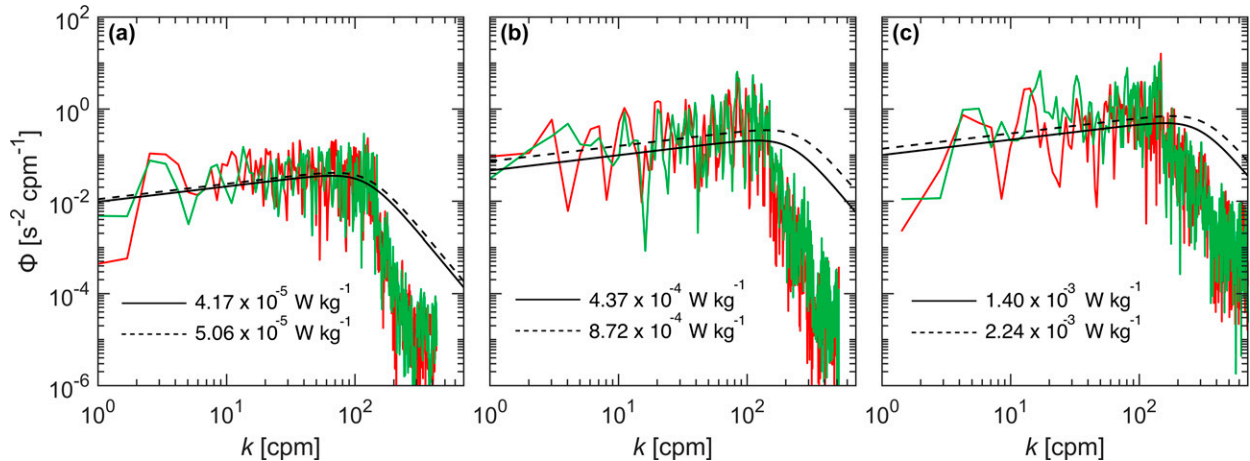


FIG. A1. Example wavenumber spectra of velocity shear from VMP-500 with TKE dissipation rate of (a) $O(10^{-5})$, (b) $O(10^{-4})$, and (c) $O(10^{-3})$ W kg^{-1} . The red and green lines are the spectral curves of shear probes 1 and 2, respectively. The solid and dashed lines are the best-fit Nasmyth empirical spectra for shear probes 1 and 2, respectively.

transition that spawns the intermediate layer sandwiched by two free shear layers, the lee waves and warm depression. Therefore, the marginal instability status of shear and observed KH billows provide evidence that mixing is linked to the collapse of the shear instability. In addition, convective instability could occur because of the entrainment between the two interfaces and the distortion of lee waves due to advection. Distortion of lee waves can also trigger the KH instability, as shown in Figs. 8 and 9. Our estimated eddy diffusivity K_ρ is concentrated in a range of high values, from $O(10^{-4})$ to $O(10^{-3})$ $\text{m}^2 \text{s}^{-1}$, and has a maximum value of 10^1 $\text{m}^2 \text{s}^{-1}$. Approximately 36% of the K_ρ is larger than the regional hydrographic data-deduced mean value of 10^{-3} $\text{m}^2 \text{s}^{-1}$ in the Kuroshio east of Taiwan (Mensah et al. 2014).

Acknowledgments. The authors thank the officers and crew on R/V *Ocean Researcher 2 (OR2)* and R/V *New Ocean Researcher 2 (NOR2)*. Field work was aided by the hard work of Wang-Ting Hsieh, Wen-Hua Her, Hsiang-Chih Hsieh, Shih-Hong Wang, Bee Wang, Wei-Ting Hung, Sin-Ya Jheng, Meng-Chao Heieh, and Chieh-Yuan Tsai. Prof. Takeyoshi Nagai greatly helped the training of the UCTD deployment of our team. We thank the editor and two anonymous reviewers whose comments significantly improved the original manuscript. MHC, YJY and SJ were supported by MOST Grants 110-2611-M-002-002, 108-2611-M-002-018 and 110-2611-M-002-026, respectively. YHC was supported by the CWB of Taiwan through Grant 1092037C and MOST Grant 110-2611-M-019-020. T. Matsuno, T. Endoh, E. Tsutsumi, and X. Guo were supported by the Ministry of Education, Culture, Sports, Science and Technology (MEXT) of Japan (15H05821), and S. Jan and T. Endoh were supported by the Collaborative Research Program of Research Institute for Applied Mechanics (RIAM), Kyushu University (18EA-2, 19EA-3, and 20EA-2).

Data availability statement. The remote sensing data of SST can be obtained from <https://oceandata.sci.gsfc.nasa.gov/>.

The Ssalto/Duacs altimeter data can be obtained from the Copernicus Marine and Environment Monitoring Service (CMEMS) (<http://www.marine.copernicus.eu>). The bathymetry data used here were provided by the MOST Ocean Data Bank (<http://www.odb.ntu.edu.tw/en/>). Data drawn from ship-based and moored measurements used to produce the figures can be obtained from the Zenodo repository (<https://doi.org/10.5281/zenodo.5607210>).

APPENDIX

Turbulent Velocity Shear Spectrum

Turbulent velocity shear is measured at a sample rate of 512 Hz by two airfoil probes mounted on the VMP. Based on the isotropic turbulence and Taylor's frozen hypothesis, TKE dissipation rate ϵ is estimated from the VMP measurements of vertical turbulent velocity shear $\partial u'/\partial z$ as

$$\epsilon = \frac{15}{2} \nu \overline{\left(\frac{\partial u'}{\partial z}\right)^2} = \frac{15}{2} \nu \int \phi(k) dk, \quad (\text{A1})$$

where ν is the molecular viscosity, $\overline{(\partial u'/\partial z)^2}$ is turbulent shear variance, $\phi(k)$ is the shear spectrum, and k is the vertical wavenumber. The ϵ is obtained by integrating the velocity shear spectra. Details for performing the integration and correction can be found in Lueck (2016). Three examples of shear spectra having TKE dissipation rate $O(10^{-5})$, $O(10^{-4})$, and $O(10^{-3})$ W kg^{-1} are shown in Figs. A1a–c, respectively. The Nasmyth spectral curves (black solid and dashed lines in Fig. A1) are used to supplement shear variance not captured by the airfoil probe at higher wavenumbers and to check on shear data quality. Compared with the Nasmyth spectra, the attenuation of probe signal at high wavenumber ($k > 150$ cpm) can be found. It is induced by the combined effect of 1) limited spatial resolution of the shear probe (Macoun and Lueck 2004; Lueck 2016) and

2) the cutoff frequency (98 Hz) of the antialiasing filter (Lueck 2016). The former is because of the finite size of the airfoil probe that makes it spatially average the velocity fluctuations at eddy size comparable to the width of the probe. Aside from the high wavenumber regime, the measured turbulent shear spectra show a good agreement with the Nasmyth empirical shear spectra, particularly in the inertial subrange, where the slope is $\sim k^{1/3}$. The shear spectrum for $O(10^{-5})$ W kg^{-1} (Fig. A1a) resolves both the inertial subrange and a part of the viscous subrange, i.e., the roll-off of the Nasmyth spectrum. The spectra for $O(10^{-4})$ and $O(10^{-3})$ W kg^{-1} (Figs. A1b,c) resolve only the inertial subrange since the shear spectrum shifts to larger wavenumbers as ϵ increases (Macoun and Lueck 2004). Practically, an accurate fitting of the shear spectra at higher wavenumbers in the viscous subrange is not critically required for the estimates of ϵ . Previous measurements of high ϵ values were obtained mainly by fitting the Nasmyth spectrum to the inertial subrange of the spectrum (e.g., Wesson and Gregg 1994; McPherson et al. 2019). Overall, our estimates of ϵ using shear spectra are acceptable.

The possible limitation to measuring a high ϵ value using VMP-500 is further discussed. The total velocity relative to the shear probe is a vector sum of the instrument falling speed W and the total cross-stream velocity fluctuations, i.e., the turbulent velocity scale u' . The angle of attack $\alpha = \tan^{-1}(u'/W)$ should be smaller than 20° for the shear probe to linearly respond to cross-stream velocity fluctuations (Lueck 2016). The turbulent velocity scale can be inferred from the measured TKE dissipation rate using $u' = (\epsilon L)^{1/3}$ (Tennekes and Lumley 1972), where L is the integral length scale (scale of energy-containing eddy). Therefore, the largest u' (and α) at a constant ϵ will originate from eddies having a scale comparable to the length of VMP-500 (1.5 m) because the larger eddies will advect the entire instrument. Assuming the measured ϵ is induced by the largest eddies ($L \sim 1.5$ m), the ϵ value 2.24×10^{-3} W kg^{-1} (Fig. A1c) corresponds to $u' = 0.15$ m s^{-1} . Given the falling speed of 0.35 m s^{-1} , α is 23° , larger than the critical value. The high TKE dissipation rate $O(10^{-3})$ W kg^{-1} appears at four data points recorded in the slow falling speed ($W \sim 0.3\text{--}0.4$ m s^{-1}) due to the strong horizontal current drag. The combination of high ϵ and low W makes α comparable to or larger than 20° . The above discussion suggests that the measured ϵ $O(10^{-3})$ W kg^{-1} could be problematic and, therefore, is removed from our analysis. Statistically, the peak turbulent velocity scale could be 3 times of u' . If we adopt the strict condition, this will make part of ϵ measurements $O(10^{-4})$ W kg^{-1} having α larger than 20° . However, this may be overcorrected because 1) we have assumed a “largest” eddy size comparable to the instrument length and 2) the shear spectra generally well fit the inertial subrange.

REFERENCES

- Acabado, C. S., Y.-H. Cheng, M.-H. Chang, and C.-C. Chen, 2021: Vertical nitrate flux induced by Kelvin-Helmholtz billows over a seamount in the Kuroshio. *Front. Mar. Sci.*, **8**, 680729, <https://doi.org/10.3389/fmars.2021.680729>.
- Aguilar, D. A., and B. R. Sutherland, 2006: Internal wave generation from rough topography. *Phys. Fluids*, **18**, 066603, <https://doi.org/10.1063/1.2214538>.
- Alford, M. H., J. B. Girton, G. Voet, G. S. Carter, J. B. Mickett, and J. M. Klymak, 2013: Turbulent mixing and hydraulic control of abyssal water in the Samoan Passage. *Geophys. Res. Lett.*, **40**, 4668–4674, <https://doi.org/10.1002/grl.50684>.
- , J. M. Klymak, and G. S. Carter, 2014: Breaking internal lee waves at Kaena Ridge, Hawaii. *Geophys. Res. Lett.*, **41**, 906–912, <https://doi.org/10.1002/2013GL059070>.
- Armi, L., and D. M. Farmer, 1986: Maximal two-layer exchange through a contraction with barotropic net flow. *J. Fluid Mech.*, **164**, 27–51, <https://doi.org/10.1017/S0022112086002458>.
- , and —, 2002: Stratified flow over topography: Bifurcation fronts and transition to the uncontrolled state. *Proc. Roy. Soc. London*, **458A**, 513–538, <https://doi.org/10.1098/rspa.2001.0887>.
- Baines, P. G., 1987: Upstream blocking and airflow over mountains. *Annu. Rev. Fluid Mech.*, **19**, 75–97, <https://doi.org/10.1146/annurev.fl.19.010187.000451>.
- Bell, T. H., 1975: Topographically generated internal waves in the open ocean. *J. Geophys. Res.*, **80**, 320–327, <https://doi.org/10.1029/JC080i003p00320>.
- Chang, M.-H., 2021: Marginal instability within internal solitary waves. *Geophys. Res. Lett.*, **48**, e2021GL092616, <https://doi.org/10.1029/2021GL092616>.
- , T. Y. Tang, C.-R. Ho, and S.-Y. Chao, 2013: Kuroshio-induced wake in the lee of Green Island off Taiwan. *J. Geophys. Res. Oceans*, **118**, 1508–1519, <https://doi.org/10.1002/jgrc.20151>.
- , S.-Y. Jheng, and R.-C. Lien, 2016: Trains of large Kelvin-Helmholtz billows observed in the Kuroshio above a seamount. *Geophys. Res. Lett.*, **43**, 8654–8661, <https://doi.org/10.1002/2016GL069462>.
- , S. Jan, V. Mensah, M. Andres, L. Rainville, Y. J. Yang, and Y.-H. Cheng, 2018: Zonal migration and transport variations of the Kuroshio east of Taiwan induced by eddy impingements. *Deep-Sea Res. I*, **131**, 1–15, <https://doi.org/10.1016/j.dsr.2017.11.006>.
- , —, C.-L. Liu, Y.-H. Cheng, and V. Mensah, 2019: Observations of island wakes at high Rossby numbers: Evolution of submesoscale vortices and free shear layers. *J. Phys. Oceanogr.*, **49**, 2997–3016, <https://doi.org/10.1175/JPO-D-19-0035.1>.
- , and Coauthors, 2021: Direct measurements reveal instabilities and turbulence within large amplitude internal solitary waves beneath the ocean. *Commun. Earth Environ.*, **2**, 15, <https://doi.org/10.1038/s43247-020-00083-6>.
- Chen, C. T. A., 2005: Tracing tropical and intermediate waters from the South China Sea to the Okinawa Trough and beyond. *J. Geophys. Res.*, **110**, C05012, <https://doi.org/10.1029/2004JC002494>.
- Cheng, Y.-H., C.-R. Ho, Q. Zheng, B. Qui, J. Hu, and N.-J. Kuo, 2017: Statistical features of eddies approaching the Kuroshio east of Taiwan Island and Luzon Island. *J. Oceanogr.*, **73**, 427–438, <https://doi.org/10.1007/s10872-017-0411-7>.
- , M.-H. Chang, D. S. Ko, S. Jan, M. Andres, A. Kirincich, Y. J. Yang, and J.-H. Tai, 2020: Submesoscale eddy and frontal instabilities in the Kuroshio interacting with a cape south of Taiwan. *J. Geophys. Res. Oceans*, **124**, e2020JC016123, <https://doi.org/10.1029/2020JC016123>.
- Cushman-Roisin, B., and J. M. Beckers, 2011: Stratification. *Introduction to Geophysical Fluid Dynamics*, Academic Press, 319–335.

- Dillon, T. M., 1982: Vertical overturns: A comparison of Thorpe and Ozmidov length scales. *J. Geophys. Res.*, **87**, 9601–9613, <https://doi.org/10.1029/JC087iC12p09601>.
- Douglas, W., and R. Lueck, 2015: ODAS MATLAB library technical manual, version 4.0. Rockland Scientific International Inc., <https://rocklandscientific.com>.
- Endoh, T., Y. Yoshikawa, T. Matsuno, Y. Wakata, K.-J. Lee, and L. Umlauf, 2016: Observational evidence for tidal straining over a sloping continental shelf. *Cont. Shelf Res.*, **117**, 12–19, <https://doi.org/10.1016/j.csr.2016.01.018>.
- Farmer, D. M., and L. Armi, 1999: Stratified flow over topography: The role of small-scale entrainment and mixing in flow reestablishment. *Proc. Roy. Soc. London*, **455A**, 3221–3258, <https://doi.org/10.1098/rspa.1999.0448>.
- Galbraith, P. S., and D. E. Kelley, 1996: Identifying overturns in CTD profiles. *J. Atmos. Oceanic Technol.*, **13**, 688–702, [https://doi.org/10.1175/1520-0426\(1996\)013<0688:IOICP>2.0.CO;2](https://doi.org/10.1175/1520-0426(1996)013<0688:IOICP>2.0.CO;2).
- Geyer, W. R., A. C. Lavery, M. E. Scully, and J. H. Trowbridge, 2010: Mixing by shear instability at high Reynolds number. *Geophys. Res. Lett.*, **37**, L22607, <https://doi.org/10.1029/2010GL045272>.
- Gregg, M. C., and L. J. Pratt, 2010: Flow and hydraulics near the sill of Hood Canal, a strongly sheared, continuously stratified fjord. *J. Phys. Oceanogr.*, **40**, 1087–1105, <https://doi.org/10.1175/2010JPO4312.1>.
- , and J. M. Klymak, 2014: Mode-2 hydraulic control of flow over a small ridge on a continental shelf. *J. Geophys. Res. Oceans*, **119**, 8093–8108, <https://doi.org/10.1002/2014JC010043>.
- Hasegawa, D., H. Yamazaki, R. G. Lueck, and L. Seuront, 2004: How islands stir and fertilize the upper ocean. *Geophys. Res. Lett.*, **31**, L16303, <https://doi.org/10.1029/2004GL020143>.
- , and Coauthors, 2021: How a small reef in the Kuroshio cultivates the ocean. *Geophys. Res. Lett.*, **48**, e2020GL092063, <https://doi.org/10.1029/2020GL092063>.
- Howard, L. N., 1961: Note on a paper by J. W. Miles. *J. Fluid Mech.*, **10**, 509–512, <https://doi.org/10.1017/S0022112061000317>.
- Jan, S., D. D. Sheu, and H.-M. Kuo, 2006: Water mass and throughflow transport variability in the Taiwan Strait. *J. Geophys. Res.*, **111**, C12012, <https://doi.org/10.1029/2006JC003656>.
- , and Coauthors, 2013: Observations of a freshwater pulse induced by Typhoon Morakot off the northern coast of Taiwan in August 2009. *J. Mar. Res.*, **71**, 19–46, <https://doi.org/10.1357/002224013807343452>.
- , and Coauthors, 2015: Large variability of the Kuroshio at 23.75°N east of Taiwan. *J. Geophys. Res. Oceans*, **120**, 1825–1840, <https://doi.org/10.1002/2014JC010614>.
- , V. Mensah, M. Andres, M.-H. Chang, and Y. J. Yang, 2017: Eddy–Kuroshio interactions: Local and remote effects. *J. Geophys. Res. Oceans*, **122**, 9744–9764, <https://doi.org/10.1002/2017JC013476>.
- , S.-H. Wang, K.-C. Yang, Y. J. Yang, and M.-H. Chang, 2019: Glider observations of interleaving layers beneath the Kuroshio primary velocity core east of Taiwan and analyses of underlying dynamics. *Sci. Rep.*, **9**, 11401, <https://doi.org/10.1038/s41598-019-47912-z>.
- Klymak, J. M., and M. C. Gregg, 2004: Tidally generated turbulence over the Knight Inlet Sill. *J. Phys. Oceanogr.*, **34**, 1135–1151, [https://doi.org/10.1175/1520-0485\(2004\)034<1135:TGTOTK>2.0.CO;2](https://doi.org/10.1175/1520-0485(2004)034<1135:TGTOTK>2.0.CO;2).
- , R. Pinkel, and L. Rainville, 2008: Direct breaking of the internal tide near topography: Kaena Ridge, Hawaii. *J. Phys. Oceanogr.*, **38**, 380–399, <https://doi.org/10.1175/2007JPO3728.1>.
- Kobari, T., and Coauthors, 2020: Phytoplankton growth and consumption by microzooplankton stimulated by turbulent nitrate flux suggest rapid trophic transfer in the oligotrophic Kuroshio. *Biogeosciences*, **17**, 2441–2452, <https://doi.org/10.5194/bg-17-2441-2020>.
- Kunze, E., and R.-C. Lien, 2019: Energy sinks for lee waves in shear flow. *J. Phys. Oceanogr.*, **49**, 2851–2865, <https://doi.org/10.1175/JPO-D-19-0052.1>.
- , E. Firing, J. M. Hummon, T. K. Chereskin, and A. M. Thurnherr, 2006: Global abyssal mixing inferred from lowered ADCP shear and CTD strain profiles. *J. Phys. Oceanogr.*, **36**, 1553–1576, <https://doi.org/10.1175/JPO2926.1>.
- Legg, S., 2021: Mixing by oceanic lee waves. *Annu. Rev. Fluid Mech.*, **53**, 173–201, <https://doi.org/10.1146/annurev-fluid-051220-043904>.
- Lian, Q., W. D. Smyth, and Z. Liu, 2020: Numerical computation of instabilities and internal waves from in situ measurements via the viscous Taylor–Goldstein problem. *J. Atmos. Oceanic Technol.*, **37**, 759–776, <https://doi.org/10.1175/JTECH-D-19-0155.1>.
- Lien, R.-C., T. B. Sanford, S. Jan, M.-H. Chang, and B. B. Ma, 2013: Internal tides on the East China Sea continental slope. *J. Mar. Res.*, **71**, 151–185, <https://doi.org/10.1357/002224013807343461>.
- , B. Ma, Y.-H. Cheng, C.-R. Ho, B. Qiu, C. M. Lee, and M.-H. Chang, 2014: Modulation of Kuroshio transport by mesoscale eddies at the Luzon Strait entrance. *J. Geophys. Res. Oceans*, **119**, 2129–2142, <https://doi.org/10.1002/2013JC009548>.
- Liu, Z., S. A. Thorpe, and W. D. Smyth, 2012: Instability and hydraulics of turbulent stratified shear flows. *J. Fluid Mech.*, **695**, 235–256, <https://doi.org/10.1017/jfm.2012.13>.
- Lueck, R., 2016: Calculating the rate of dissipation of turbulent kinetic energy. Rockland Scientific International Tech. Note TN-028, 19 pp., <https://rocklandscientific.com/wp-content/uploads/2021/12/TN-028-Calculating-the-Rate-of-Dissipation-of-Turbulent-Kinetic-Energy.pdf>.
- MacKinnon, J. A., and Coauthors, 2017: Climate process team on internal wave–driven ocean mixing. *Bull. Amer. Meteor. Soc.*, **98**, 2429–2454, <https://doi.org/10.1175/BAMS-D-16-0030.1>.
- Macoun, P., and R. Lueck, 2004: Modelling the spatial response of the airfoil shear probe using different sized probes. *J. Atmos. Oceanic Technol.*, **21**, 284–297, [https://doi.org/10.1175/1520-0426\(2004\)021<0284:MTSROT>2.0.CO;2](https://doi.org/10.1175/1520-0426(2004)021<0284:MTSROT>2.0.CO;2).
- McPherson, R. A., C. L. Stevens, and J. M. O’Callaghan, 2019: Turbulent scales observed in a river plume entering a fjord. *J. Geophys. Res. Oceans*, **124**, 9190–9208, <https://doi.org/10.1029/2019JC015448>.
- Mensah, V., S. Jan, M.-D. Chiou, T.-H. Kuo, and R.-C. Lien, 2014: Evolution of the Kuroshio tropical water from the Luzon Strait to the east of Taiwan. *Deep-Sea Res. I*, **86**, 68–81, <https://doi.org/10.1016/j.dsr.2014.01.005>.
- Miles, J. W., 1961: On the stability of heterogeneous shear flows. *J. Fluid Mech.*, **10**, 496–508, <https://doi.org/10.1017/S0022112061000305>.
- Moum, J. N., 2021: Variations in ocean mixing from seconds to years. *Annu. Rev. Mar. Sci.*, **13**, 201–226, <https://doi.org/10.1146/annurev-marine-031920-122846>.
- , and J. D. Nash, 2000: Topographically induced drag and mixing at a small bank on the continental shelf. *J. Phys. Oceanogr.*, **30**, 2049–2054, [https://doi.org/10.1175/1520-0485\(2000\)030<2049:TIDAMA>2.0.CO;2](https://doi.org/10.1175/1520-0485(2000)030<2049:TIDAMA>2.0.CO;2).

- Musgrave, R. C., MacKinnon, J. A., Pinkel, R., Waterhouse, A. F., and Nash, J. D., 2016: Tidally driven processes leading to near-field turbulence in a channel at the crest of the Mendocino Escarpment. *J. Phys. Oceanogr.*, **46**, 1137–1155, <https://doi.org/10.1175/JPO-D-15-0021.1>.
- Nagai, T., D. Hasegawa, T. Tanaka, H. Nakamura, E. Tsutsumi, R. Inoue, and T. Yamashiro, 2017: First evidence of coherent bands of strong turbulent layers associated with high-wavenumber internal-wave shear in the upstream Kuroshio. *Sci. Rep.*, **7**, 14555, <https://doi.org/10.1038/s41598-017-15167-1>.
- , and Coauthors, 2021: The Kuroshio flowing over seamounts and associated submesoscale flows drive 100-km-wide 100-1000-fold enhancement of turbulence. *Commun. Earth Environ.*, **2**, 170, <https://doi.org/10.1038/s43247-021-00230-7>.
- Nash, J. D., and J. N. Moum, 2001: Internal hydraulic flows over the continental shelf: High drag states over a small bank. *J. Geophys. Res.*, **106**, 4593–4611, <https://doi.org/10.1029/1999JC000183>.
- Nikurashin, M., and R. Ferrari, 2011: Global energy conversion rate from geostrophic flows into internal lee waves in the deep ocean. *Geophys. Res. Lett.*, **38**, L08610, <https://doi.org/10.1029/2011GL046576>.
- Osborn, T. R., 1980: Estimates of the local rate of vertical diffusion from dissipation measurements. *J. Phys. Oceanogr.*, **10**, 83–89, [https://doi.org/10.1175/1520-0485\(1980\)010<0083:EOTLRO>2.0.CO;2](https://doi.org/10.1175/1520-0485(1980)010<0083:EOTLRO>2.0.CO;2).
- Pratt, L. J., H. E. Deese, S. P. Murray, and W. Johns, 2000: Continuous dynamical modes in straits having arbitrary cross sections, with applications to the Bab al Mandab. *J. Phys. Oceanogr.*, **30**, 2515–2534, [https://doi.org/10.1175/1520-0485\(2000\)030<2515:CDMISH>2.0.CO;2](https://doi.org/10.1175/1520-0485(2000)030<2515:CDMISH>2.0.CO;2).
- Smyth, W. D., 2020: Marginal instability and the efficiency of ocean mixing. *J. Phys. Oceanogr.*, **50**, 2141–2150, <https://doi.org/10.1175/JPO-D-20-0083.1>.
- , and J. R. Carpenter, 2019: *Instability in Geophysical Flows*. Cambridge University Press, 328 pp.
- St. Laurent, L., A. C. Naveira Garabato, J. R. Ledwell, A. M. Thurnherr, J. M. Toole, and A. J. Watson, 2012: Turbulence and diapycnal mixing in Drake Passage. *J. Phys. Oceanogr.*, **42**, 2143–2152, <https://doi.org/10.1175/JPO-D-12-027.1>.
- Tanaka, T., D. Hasegawa, T. Okunishi, H. Kaneko, and T. Ono, 2021: Internal hydraulic jump in the Tsugaru Strait. *J. Oceanogr.*, **77**, 215–228, <https://doi.org/10.1007/s10872-020-00588-w>.
- Tennekes, H., and J. L. Lumley, 1972: *A First Course in Turbulence*. MIT Press, 300 pp.
- Thorpe, S. A., 1977: Turbulence and mixing in a Scottish loch. *Philos. Trans. Roy. Soc. London*, **286A**, 125–181, <https://doi.org/10.1098/rsta.1977.0112>.
- , and Z. Liu, 2009: Marginal instability? *J. Phys. Oceanogr.*, **39**, 2373–2381, <https://doi.org/10.1175/2009JPO4153.1>.
- Tsutsumi, E., T. Matsuno, R.-C. Lien, H. Nakamura, T. Senjyu, and X. Guo, 2017: Turbulent mixing within the Kuroshio in the Tokara Strait. *J. Geophys. Res. Oceans*, **122**, 7082–7094, <https://doi.org/10.1002/2017JC013049>.
- Wesson, J. C., and M. C. Gregg, 1994: Mixing at Camarinal Sill in the Strait of Gibraltar. *J. Geophys. Res.*, **99**, 9847–9878, <https://doi.org/10.1029/94JC00256>.
- Winters, K. B., 2016: The turbulent transition of a supercritical downslope flow: Sensitivity to downstream conditions. *J. Fluid Mech.*, **792**, 997–1012, <https://doi.org/10.1017/jfm.2016.113>.
- Xie, X., and M. Li, 2019: Generation of internal lee waves by lateral circulation in a coastal plain estuary. *J. Phys. Oceanogr.*, **49**, 1687–1697, <https://doi.org/10.1175/JPO-D-18-0142.1>.